中文摘要

隨著光儲存等應用系統的迅速發展，微光點的量測變得越來越迫切和重要，利用傳統的遠場光學方法並不能直接量測聚焦光點，且解析度受限於光感測器的像素大小(約 5 μm)。然而，使用近場光學量測卻因為要將物體擺設在待測光場的近場範圍內，系統架設複雜、高成本又不易實現即時量測，而且其解析度也受限於探針的孔徑。因此，為了提供高解析度、降低成本又方便使用的微光點量測方法，我們提出了一種利用掃瞄刀緣法(scanning knife-edge method)的微光點大小及形狀量測系統，整合了梳狀致動器、光感測器和平整的刀緣掃瞄板以直接對微光點作量測。

為了實現此一系統，我們選擇了透過 SOI 和可以整合電路的 CMOS 後製程兩方面作為目標前進，在本文中，成功的利用 SOI 整合了上述元件並提出了一個新的背向乾蝕刻方式去改善良率，我們也對完成的元件作測試和討論，包括致動器動態響應和光感測器的響應度。另外，透過 CIC 的製程服務，設計並佈局的 CMOS 製程中整合了上述元件和電路，經過了測試實驗，也驗證了所提出 CMOS 後製程的可行性。

最後，我們將完成的反射式和吸收式 SOI 元件對雷射聚焦光點大小作量測，利用反射式元件量測的光點大小和形狀成功的驗證此一系統。在吸收式系統的量測方面，將討論面臨到的問題和改善的方向以奠定日後對微光機電整合晶片研發的基礎。

Abstract

As the optical spot size in applications such as optical data storage gets smaller, the measurements of focused laser spot become more necessary and important. In conventional far-field optical distribution, the micro spot size can not be acquired directly. The measurements performed by near-field scanning optical microscopes (NSOM) are more complex and costly because the detector must be placed in the near-field proximity. Therefore, a microelectromachanical system (MEMS) optical spot profile measurement system based on the scanning knife-edge technique is proposed. In the fabricated device, a knife-edge plate and a photo detector are integrated on the micro actuator to scan across the optical distribution.

The fabrications are performed by using SOI (silicon-on-insulator) MEMS and CMOS (complementary-metal-oxide-semiconductor) MEMS. In the thesis, a new approach is proposed for SOI process to dry etching the backside silicon. The fabricated components, including comb actuator and photo detector, are measured and discussed. The CMOS device is also designed to attempt a fully integration with circuits. By the test experiments, the feasibility of the proposed CMOS post processes is verified.

At last, the focused laser spot measurements are performed by the SOI device. The obtained spot size and profile shows a good agreement to the theoretical value and demonstrate the system. In the absorption type, the encountered problems are discussed to provide fundamentals for further researches.

致謝

結束了碩士班的研究生活，謹懷著感激的心謝謝大家，首先要感謝的是我的指導教授邱一博士，他給了我許多很棒的專業指導和建議，每每帶領我走出錯誤的觀念和認知，使實驗成果能一直順利的延續和累積，回想這兩年來的日子，當需要老師幫忙和指導的時候，老師總是不斷的伸出援手，不論是研究表現和學習狀況，讓我都能有超越自己能力的演出，希望這些表現在畢業之後還會發生，另外，也很感謝老師對實驗室的努力經營，讓我們能在製程和量測方面，都能考量成果優先，不侷限於經費，謝謝老師讓我體會到研究的感覺。

非常感謝我的口試委員，邱俊誠主任、盧向成老師和黃聖傑老師，能在繁忙之餘對我的論文指導建議和鼓勵，讓我銘記在心。

還有感謝實驗室學長，文中、俊毅、志偉、育杉和英傑對我的指導，讓我能銜接你們步伐前進，以及邱俊誠實驗室博士班學長永峻、秦輔和冠州，謝謝你們對我在實驗上的建議和幫助，特別是冠州學長在 CMOS 部分的強力支援，讓我能排除困難，順利的設計和下線。還有感謝電子所的學長兆欽，總是全力協助我的量測部分，並且教了我很多半導體元件的知識，感謝奈米中心徐小姐、黃小姐、陳小姐和葉先生以及機械所的志柏，讓我能迅速的完成許多的製程實驗。

當然，很感動能有炯廷、建勳、忠衛和亦謙這些珍貴的實驗室伙伴，幫助我的論文和一起度過了愉快又另人難忘的實驗室生活，無論是在奈米中心和 PSOC 實驗室，每個一起打拼到半夜的日子都是充實且開心的，還有繁果、瑋智和子麟等學弟，你們都是好學弟也希望你們能有傑出的表現。

謝謝我的爸媽，在求學的路上全力的幫助我支持我，讓我能無憂無慮的完成我的學業，還有女友宗玲，容忍我的毛病陪伴著我，總是在我低潮的時候幫助我和鼓勵我，妳真的很棒，有妳真好。最後，再次感謝大家，你們的關懷和協助是我腦海中永遠的回憶。

Table of Content

中文摘要 i

Abstract......ii

致謝......iii

Table of Content......iv

List of Figures......vi

List of Tables......viii

Chapter 1 Introduction......1

1.1 Motivation......1

1.2 Scanning knife-edge method......2

1.3 MEMS-based optical profile measurement system......4

1.4 Suspended microstructure fabrication......5

1.4.1 SOI process......5

1.4.2 CMOS process and post-CMOS fabrication......6

1.5 Literature survey......7

1.5.1 Optical spot profile measurement......7

1.5.2 Optical MEMS System......9

1.5.3 Devices in CMOS MEMS......11

1.6 Objectives and thesis organization......12

Chapter 2 Design and Analysis......14

2.1 Comb drive actuator......14

2.1.1 Spring constant......14

2.1.2 Comb drive actuator......15

2.1.3 Resonant frequency......17

2.1.4 Geometric design of SOI device......17

2.1.5 Geometric design of CMOS MEMS device......20

2.2 Photo detector......25

2.2.1 Silicon photo detector......26

2.2.2 Responsivity......27

2.3 Signal analysis of spot profile measurement......29

2.4 Conclusion......33

Chapter 3 Fabrication......34

3.1 SOI process......34

3.2 Fabrication problems in the SOI process......37

3.2.1 Al protection......37

3.2.2 Stresses effect......38

3.2.3 Backside etching 40
3.2.4 Fabricated SOI devices 44
3.3 Post CMOS process 45
3.4 Post process testing 48
3.4.1 Backside photolithography 48
3.4.2 Isotropic silicon etching 49
3.4.3 Anisotropic oxide etching 50
3.5 Summary 52
Chapter 4 Experiment Results and Measurement 53
4.1 Comb drive actuator 53
4.2 Characteristics of photo detector 55
4.3 Optical profile measurement 59
4.3.1 Reflection-type system 60
4.3.2 Absorption-type system 66
4.4 Summary 68
Chapter 5 Conclusion and Future Work 69
5.1 Conclusion 69
5.2 Future work 69
References 71

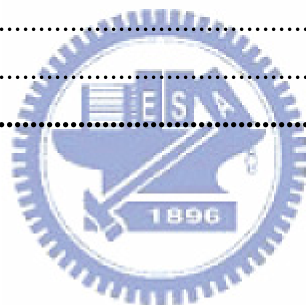

List of Figures

Fig. 1-1 CCD optical spot measurement system 1
Fig. 1-2 Schematic of near field scanning optical microscope 2
Fig. 1-3 Schematic of a scanning knife edge system 3
Fig. 1-4 Spot profile *P*(*x*') and measured signal *I*(*x*) 3
Fig. 1-5 FWHM in optical power and photocurrent distribution 4
Fig. 1-6 Top view of the micro spot profile measurement system 4
Fig. 1-7 SOI MEMS process (a) deep dry etching (b) release 5
Fig. 1-8 CMOS MEMS process 7
Fig. 1-9 images and section curves of measured focused spot 8
Fig. 1-10 (a) Knife-edge (b) Intensity distribution at the detector plane 9
Fig. 1-11 High efficiency NSOM probe 10
Fig. 1-12 Configuration of a compact optical encoder 10
Fig. 1-13 A grating-based microspectrometer 11
Fig. 1-14 A lateral-axis gyroscope 12
Fig. 1-15 A APS pixel 12
Fig. 2-1 (a) A sprig element (b) folded flexure structure 15
Fig. 2-2 Cell of engaged comb drive arrays 16
Fig. 2-3 SOI comb actuator layout 18
Fig. 2-4 Mode analysis of SOI comb actuator 20
Fig. 2-5 Cross section view of TSMC 2P4M 0.35 μm process 21
Fig. 2-6 Structure cross section view 21
Fig. 2-7 CMOS comb actuator layout 22
Fig. 2-8 Mode analysis of CMOS comb actuator 24
Fig. 2-9 Cross section view of a: (a) normal beam (b) improved beam 25
Fig. 2-10 (a) Compensation of fingers (b) top view of the full layout 25
Fig. 2-11 A p-n junction photodiode 27
Fig. 2-12 Doping profiles of p-n junction 28
Fig. 2-13 Responsivity under reverse bias voltage 29
Fig. 2-14 Driving signal *V*(*t*) and derived displacement *x*(*t*) 30
Fig. 2-15 Definition of FWHM in power and photocurrent distribution 30
Fig. 2-16 Signal processing 31
Fig. 3-1 SOI fabrication process 35
Fig. 3-2 SEM (a) etched aluminum wire (b) peeled off aluminum film 37
Fig. 3-3 Curling by residual stresses in SOI device 38
Fig. 3-4 Top view and AA' cross section view of the stressed structure 39

Fig. 3-5 SEM of (a) deflected beams (d) structure stuck on the substrate....39
Fig. 3-6 A new approach for backside etching....40
Fig. 3-7 Modified process....42
Fig. 3-8 SEM of backside etching....44
Fig. 3-9 SEM of fabricated devices....45
Fig. 3-10 Cross section view of CMOS process and components of device....46
Fig. 3-11 Post CMOS fabrication process....47
Fig. 3-12 Pattern on a CMOS chip of size 1.1×1.6 mm^2....49
Fig. 3-13 Etching profile by WYKO....49
Fig. 3-14 SEM of undercut profile for (a) 10 minutes (b) 20 minutes....50
Fig. 3-15 Cross section view of: (a) testing process (b) CMOS process....51
Fig. 3-16 SEM of the RIE grass (a) without IPA rinse (b) with IPA rinse....51
Fig. 3-17 SEM of released structure....52
Fig. 4-1 Images of (a) fabricated device (b) operation at resonance....53
Fig. 4-2 Frequency response of (a) amplitude (b) phase....54
Fig. 4-3 The width of (a) spring (b) finger....54
Fig. 4-4 Displacement under the applied voltage ($V_{DC}+V_{AC}$)....55
Fig. 4-5 Area of testing diode measured by a WYKO interferometer....56
Fig. 4-6 Measured photocurrent of: (a) first run photo detector ($N_S = 10^{17}$ cm^{-3}) (b) second run photo detector ($N_S = 10^{15}$ cm^{-3})....57
Fig. 4-7 Measured photocurrent of third run photo detector after: (a) metallization (b) ICP and release steps....57
Fig. 4-8 Area of the actual diode measured by the WYKO interferometer....58
Fig. 4-9 The I-V curve of the photo detector for absorption type....58
Fig. 4-10 Focused laser spot: (a) image (b) normalized distribution....59
Fig. 4-11 Setup of the reflective type spot profile measurement system....60
Fig. 4-12 Observed signals with a 12mW red (633 nm) light laser....61
Fig. 4-13 Observed signals with a 0.8mW green (543 nm) light laser....61
Fig. 4-14 (a) Measured photocurrent and (b) derived power distribution of the spot with 20X objective lens for the red light....62
Fig. 4-15 (a) Measured photocurrent and (b) derived power distribution of the spot with 40X objective lens for the red light....63
Fig. 4-16 (a) Measured photocurrent and (b) derived power distribution of the spot with 20X objective lens for the green light....64
Fig. 4-17 (a) Measured photocurrent and (b) derived power distribution of the spot with 40X objective lens for the green light....65
Fig. 4-18 Amplified detection setup....66
Fig. 4-19 Coupling of the absorption type device....67

List of Tables

Table 2-1 SOI comb actuator layout parameters……………………………………..19

Table 2-2 Mode frequencies of SOI device by CoventorWare……………………….20

Table 2-3 Thickness of each layers…………………...……………………………...21

Table 2-4 CMOS comb actuator layout parameters………………………………… 23

Table 3-1 Detailed SOI fabrication process…………….………………..………..36

Table 3-2 Detailed fabrication parameters of the modified SOI process….…………44

Table 3-3 Detailed fabrication parameters of test experiments.……………….……..52

Table 4-1 Measured and theoretical focused spot size………..…….……………..66

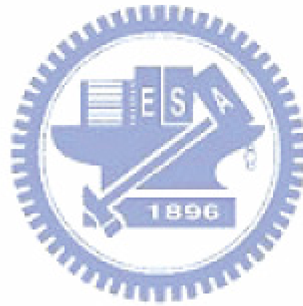

Chapter 1 Introduction

1.1 Motivation

Optical spot profile measurement is important in lens fabrication and laser beam characterization. Charge-coupled device (CCD) beam profiling systems have been widely used to capture optical beam profiles. In the CCD measurement setup shown in Fig. 1-1, the focused spot profile is acquired after the calculation from the optics specifications. However, this is a complex and bulky system and can only be used to measure the far-field optical distribution. For small scale applications such as micro- or nano-optics, near-field scanning optical microscopy (Fig. 1-2) can be used to measure optical distributions with very high resolution [1]. However, the system is also complex due to the need to detect small optical signals, and the scanning probes (or fibers) are fragile and difficult to fabricate.

Therefore, a MEMS-based optical spot profile measurement system is proposed as a more compact and robust device for near-field distribution and tight spot measurement. The proposed device has a smooth and sharp knife-edge plate. A photo

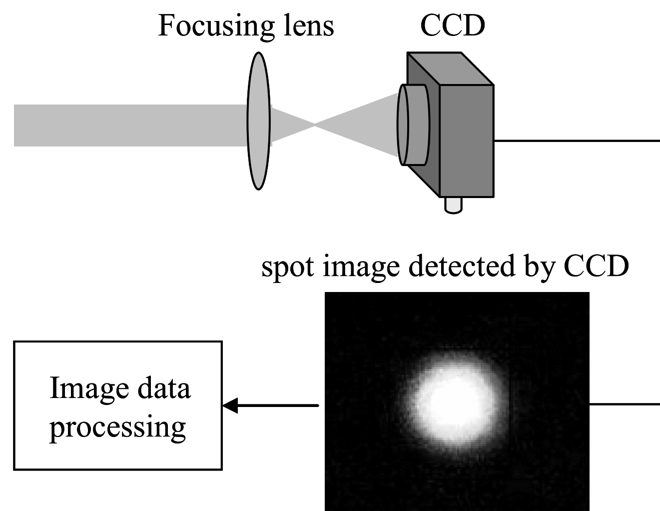

Fig. 1-1 CCD optical spot measurement system

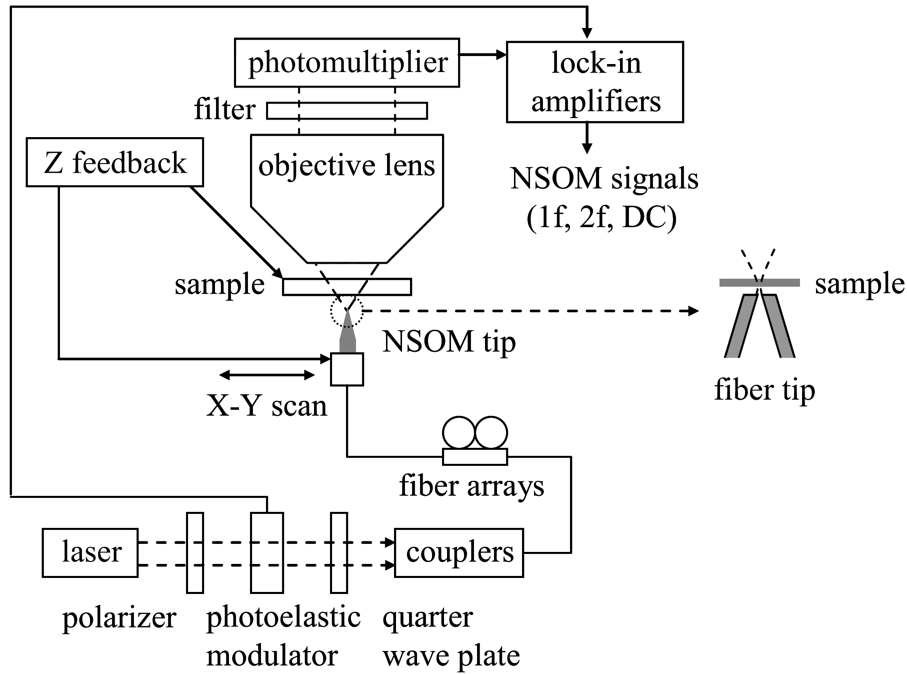

Fig. 1-2 Schematic of near field scanning optical microscope

detector fabricated on the micro actuator is used to scan across the optical field. By analyzing the electrical signals from the photo detector, the optical distribution and spot size can be determined. In the MEMS-based device, the distance between the photo detector and knife-edge plate can be less than a few μm. Alternatively, the photo detector can be fabricated on the plate. Therefore, the spatial resolution is limited by the actuator control and signal analysis, not by the diffraction limit.

The proposed micro optical spot profile measurement system is also a demonstration of an integrated optical MEMS system. The actuator, photo detector, and signal processing circuits can be integrated monolithically to form a photonic system on chip.

1.2 Scanning knife-edge method

In a scanning knife edge system as shown in Fig. 1-3, a sharp knife edge plate scans across an optical field distribution. The photo detector placed behind the plate

detects the partial optical energy which is not blocked by the plate. The photo current $I(x)$ is given by:

$$I(x) = k\int_{x}^{\infty} P(x')dx', \tag{1}$$

where x is the position of edge, $P(x)$ is the optical field distribution, and k is the sensitivity of the photo detector (Fig. 1-4). When the plate scans across the distribution, the photo current $I(x)$ is measured as function of edge position x. The optical distribution can be found from:

$$P(x) = -\frac{1}{k}\frac{dI(x)}{dx} \tag{2}$$

If the spot has a Gaussian profile, the full width at half maximum (FWHM) of the spot can be inferred from the distance between 12% and 88% of the full scale of the measured photo current $I(x)$, as shown in Fig. 1-5.

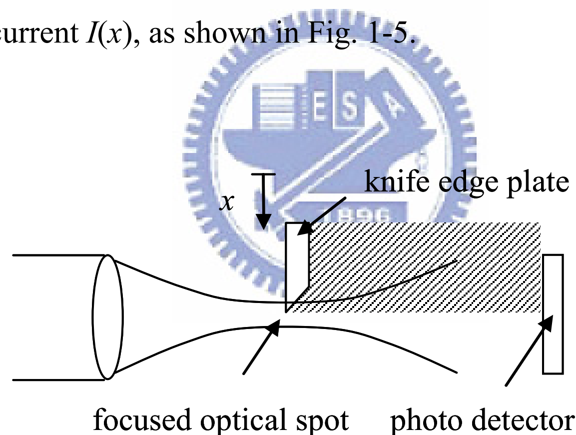

Fig. 1-3 Schematic of a scanning knife edge system

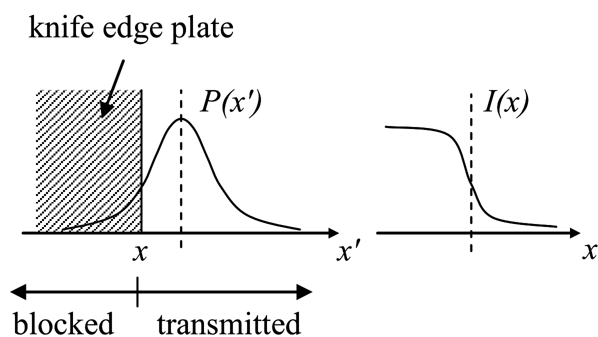

Fig. 1-4 Spot profile $P(x')$ and measured signal $I(x)$

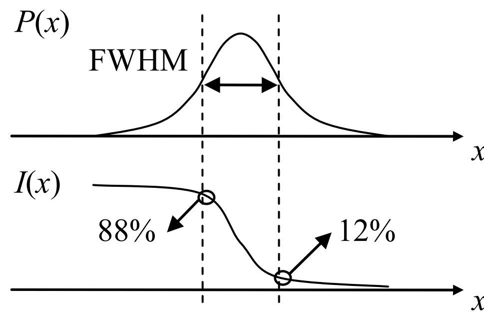

Fig. 1-5 FWHM in optical power and photocurrent distribution

1.3 MEMS-based optical profile measurement system

To implant the micro optical spot profile measurement system shown in Fig. 1-6 (a), three configurations can be considered. The first design (Fig. 1-6 (b)) is a miniaturization of the traditional system, with the photo detector placed behind the knife edge plate. In the second design (Fig. 1-6 (c)), a triangular reflective area is used as the knife edge plate. The partial light energy that is reflected from the reflective mirror is detected by a remote photo detector. In the last designed (Fig. 1-6 (d)), a

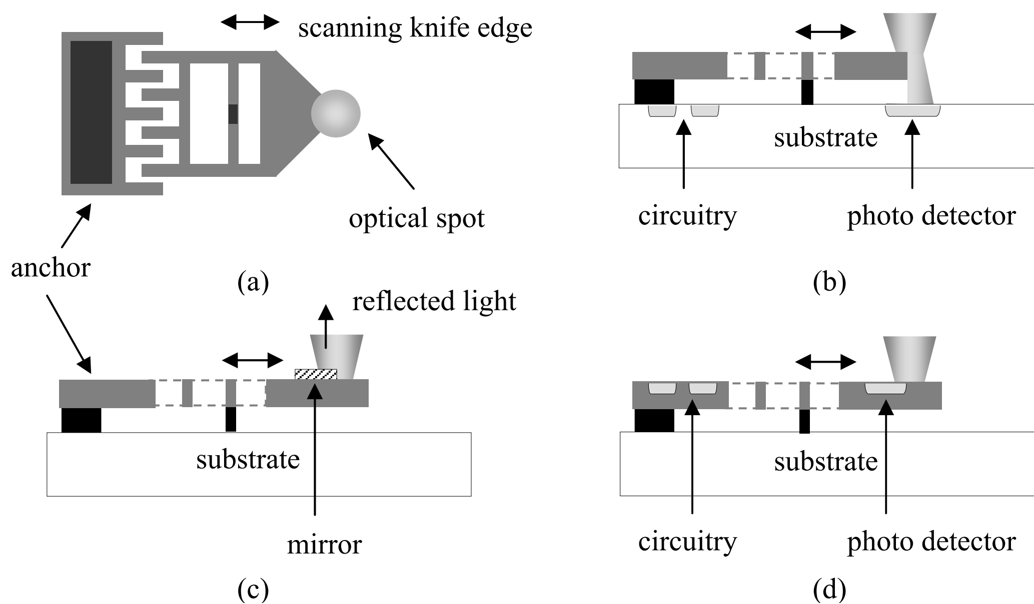

Fig. 1-6 Top view of the micro spot profile measurement system, (b) transmission

type, (c) reflection type, (d) absorption type

triangular photo detector is fabricated directly in the comb drive structure. The detector oscillates with the comb drive and serves as the knife edge plate. Among different configurations, the absorption type device is more attractive than the others by its higher integration level. Therefore, our efforts are focused on the design of the absorption type, while the reflection is also fabricated as a demonstration.

1.4 Suspended microstructure fabrication

No single process can be used to fabricate all possible MEMS. A commonly used process to fabricate the suspended microstructures is SOI MEMS. The photodetector has better performance by using single crystalline silicon (SCS), and the buried oxide provide a good solution to isolate the electrical signal between the sensor and the actuator. At the same time, CMOS MEMS is also popular because of their compatibility with circuits. Therefore, both techniques are suitable for the absorption type and will be discussed in the following sections.

1.4.1 SOI process

A SOI wafer, composed of the device layer, buried oxide, and the handle layer, is made by wafer to wafer bonding. The SOI MEMS process, illustrated in Fig. 1-7, uses the deep reactive ion etch (DRIE) process to create high-aspect-ratio silicon

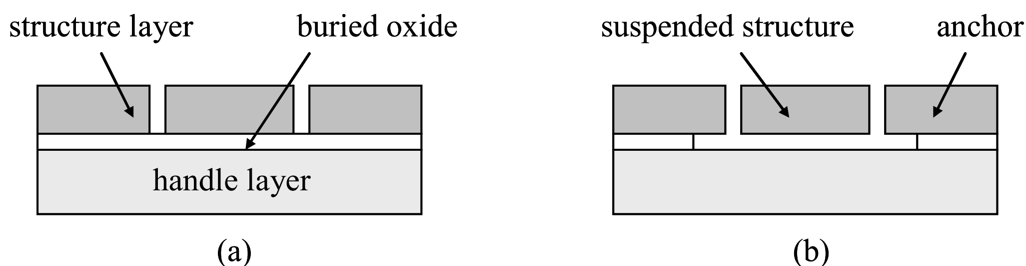

Fig. 1-7 SOI MEMS process (a) deep dry etching (b) release

suspended microstructures. Then the structures are released by a timed etch HF of the oxide spacer layer. These processes have aspects of both bulk and surface micromachining. They are popular due to the process simplicity and the ability to make SCS microstructures with thickness typically ranging from 5 to 100 μm. Electrical insulating can be accomplished by forming the device on pedestals of the underlying oxide (Fig. 1-7 (b)).

1.4.2 CMOS process and post-CMOS fabrication

MEMS applications range broadly from electronics, automobiles and imagers. The signals from the MEMS devices usually need a series of processing before readout. For a mature product, the integration of MEMS components and circuits is important for its performance, reliability, and cost. Compatibility of MEMS fabrication with mainstream integrated circuit (IC) technology provides not only those advantages but also fast economical accessibility and short design cycles.

Although MEMS leverages IC technology, many MEMS process are not compatible with the standard CMOS process. The need for extra micromachining usually leads to low yield and performance degradation. Thus, a post CMOS process is developed to make the micromachining steps truly independent of CMOS process.

Carnegie Mellon's approach uses the CMOS interconnect layers for the microstructures [2]. The wet etching and the masks are not necessary. The cross section view of a standard CMOS process is shown in Fig. 1-8 (a). The first post-micromachining step is a CHF_3:O_2 reactive ion etch (RIE) (Fig. 1-8 (b)). The top metal layer acts as a highly selective mask which defines the microstructures. After dielectric etching, silicon DRIE then sets the spacing from the suspended structure to substrate (Fig. 1-8 (c)). The last step is an isotropic etch for structure release (Fig. 1-8 (d)). All process is performed through dry etching. Various thin-film CMOS-MEMS

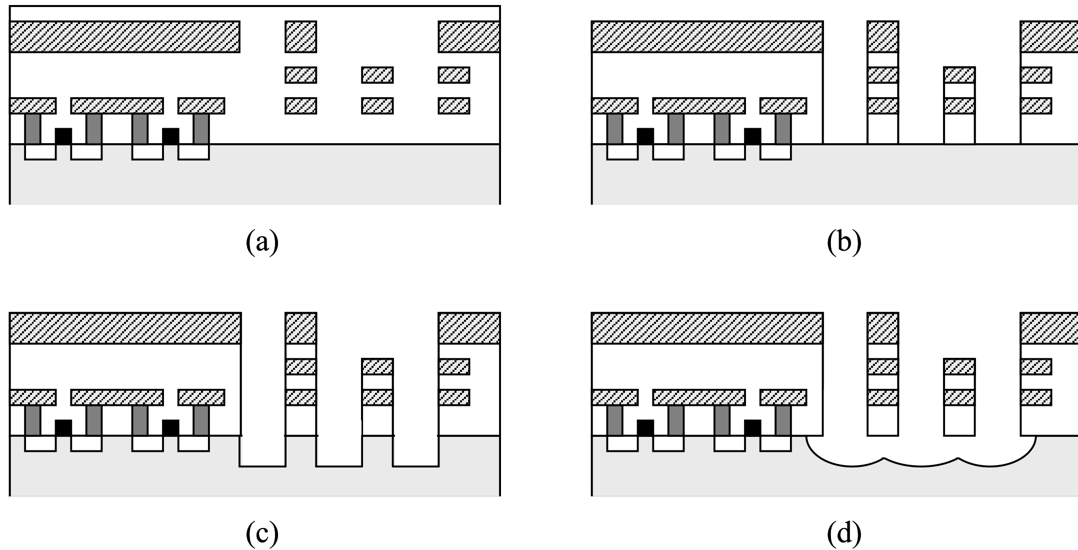

Fig. 1-8 CMOS MEMS process (a) foundry 3-metal CMOS (b) oxide RIE (c) silicon DRIE (d) isotropic silicon etch

device such as accelerometers [3], gyroscopes [4], infrared imagers [5], and microstages [6] have been demonstrated.

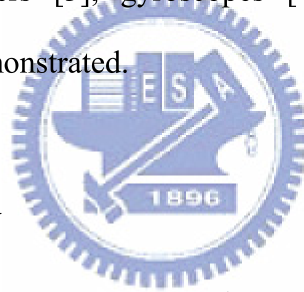

1.5 Literature survey

1.5.1 Optical spot profile measurement

In the conventional CCD measurement setup [7], the focused spot size can be acquired by the analysis of the CCD pixel array. The practical pixel, size between 5 and 15 μm limit the size of the spot that can be measured. The CCD measurement is an imaging system. The aberration of optical components can affect the accuracy. But the near-field distribution can not be measured. Therefore, some other measurement systems have been proposed to achieve better results.

A tapping-mode tuning-fork near-field scanning optical microscope is used in direct measurements of the focused spot [8]. A tapered near-field optical fiber probe of the NSOM system is used to determine the intensity profile on the focal plane. The optical distribution can be clearly recognized for different incident light sources (Fig.

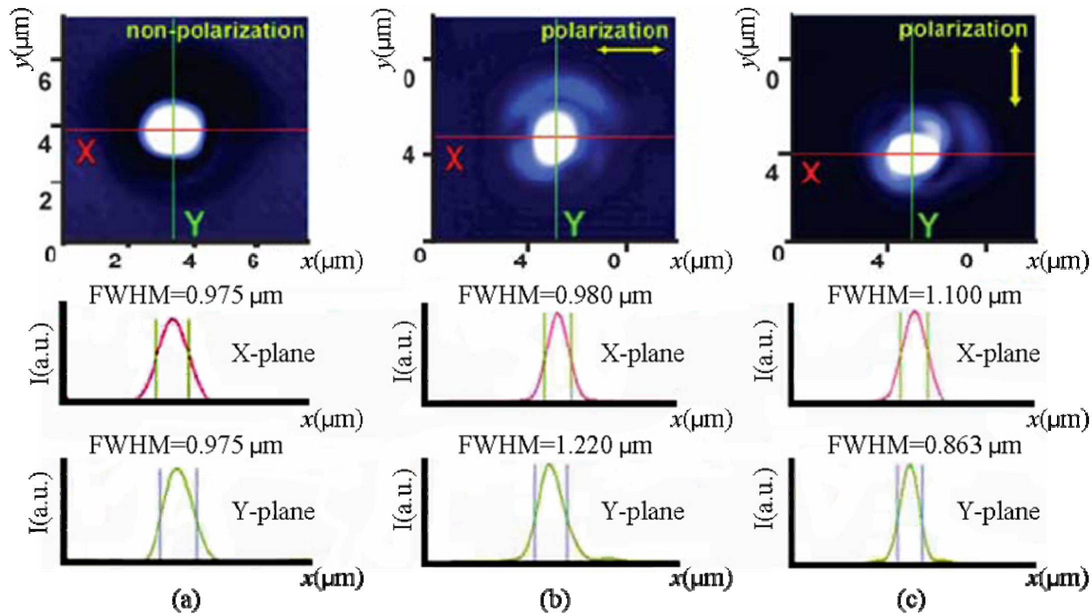

Fig. 1-9 images and section curves of measured focused spot (a) random polarized light source (b) (c) linear polarized light source along the x-axis and the y-axis [8]

1-9). Like the most of the other NSOM systems, the resolution is beyond the diffraction limit. However, the measurement set-up is even more complex than the far field CCD measurement. In many experiments, the need of real-time data can not be realized. The high cost of fiber tip and precise feedback control of stage positions are also concerns.

The knife edge method is recently become popular in the submicron spot size measurement. The knife edge can be scanned in two orthogonal axis and provides an accurate estimate of the spot size. A vibrating knife edge technique is used to detect optical distribution by Cywiak, et al. [9]. As illustrated in Fig 1-10 (a), the knife edge is placed in front of the photodiode. The electrical signal is produced by the sinusoidal vibration of the knife edge to block the beam that reaches the photodiode. The spot size is obtained from the normalized optical distribution at the detector plane shown in Fig. 1-10 (b).

Based on the above discussion, the scanning knife edge technique gives good

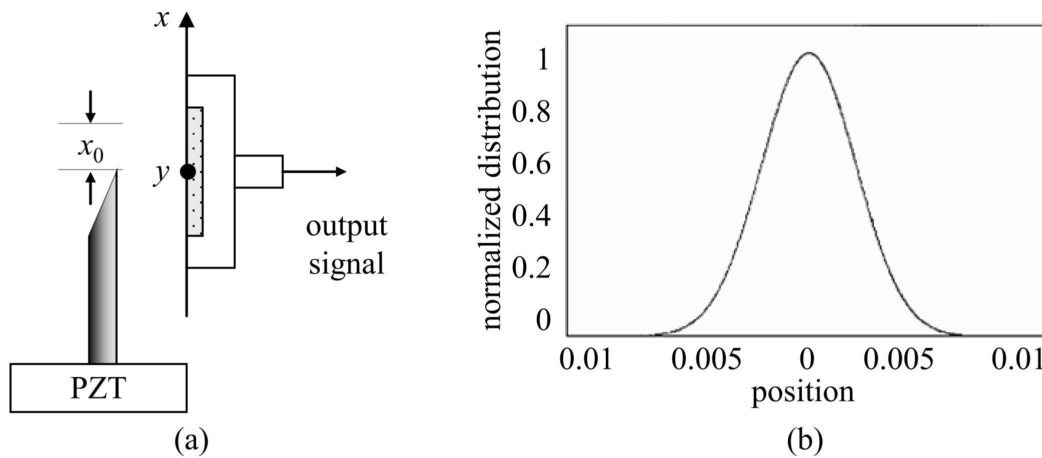

Fig. 1-10 (a) Knife-edge adjustment (b) Intensity distribution at the detector plane [9]

spatial resolution without complex and costly system. It is possible to fabricate a knife edge device using MEMS technology. Such a single chip device makes the spot size measurement more accurate and more convenient.

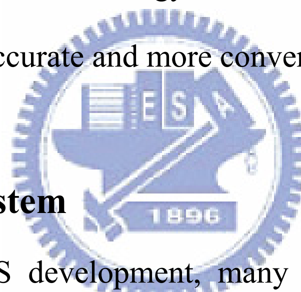

1.5.2 Optical MEMS System

In current optical-MEMS development, many researches are focused on the integration of electrical, optical, and mechanical structures. However, few of them fabricate the whole system on a single chip. The digital mirror device (DMD) [10], developed by Texas Instrument (TI) for projection display and optical communication, is an electro-mechanical system. No optical interaction or feedback is involved in this device. In the NSOM probe proposed by Sasaki, et al. [11], as shown in Fig. 1-11, the waveguide and photodiode are integrated on a cantilever beam. The integration of micromechanical structure, micro optical components and optoelectric components were demonstrated.

A compact optical encoder was proposed by Hane, et al. [12]. It is composed of an index grating, a reflection scale grating, and a photo detectors array (Fig. 1-12). The linear photodiode array is fabricated on the RIE etched silicon by ion

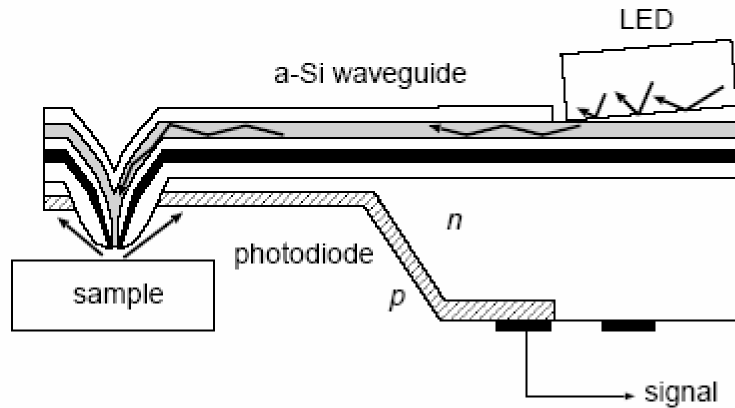

Fig. 1-11 High efficiency NSOM probe [11]

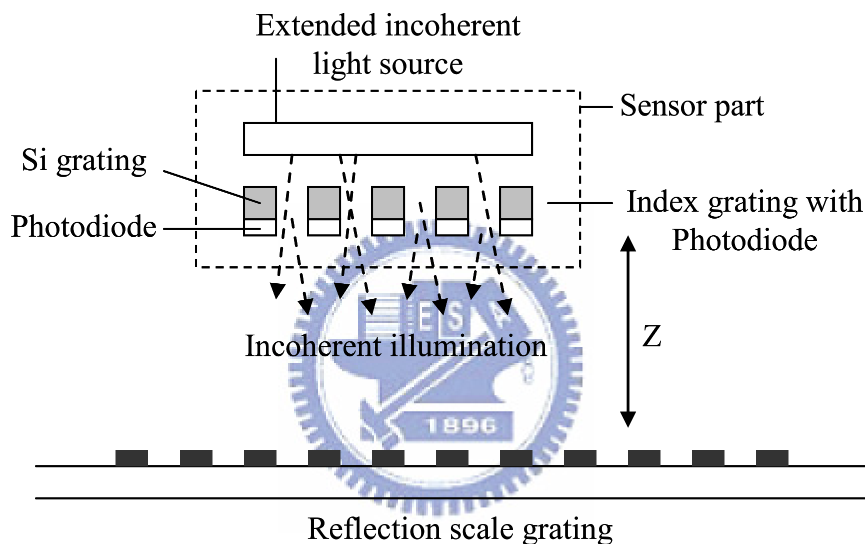

Fig. 1-12 Configuration of a compact optical encoder [12]

implantation. The displacement signal was examined while the photodiodes detect the light reflected by the scale grating attached to the fabricated device. However, no actuators was integrated on the device.

Microspectrometers have been developed for operation in various wavelength ranges. The IR microspectrometer developed by Kong, et al., [13], is shown in Fig. 1-13. Aluminum was used for multiple-silt grating. The thermopiles were used to detect the diffracted infrared light in the IR spectral range. The measurement of wavelengths can be easily implemented. The two independently processed wafers can

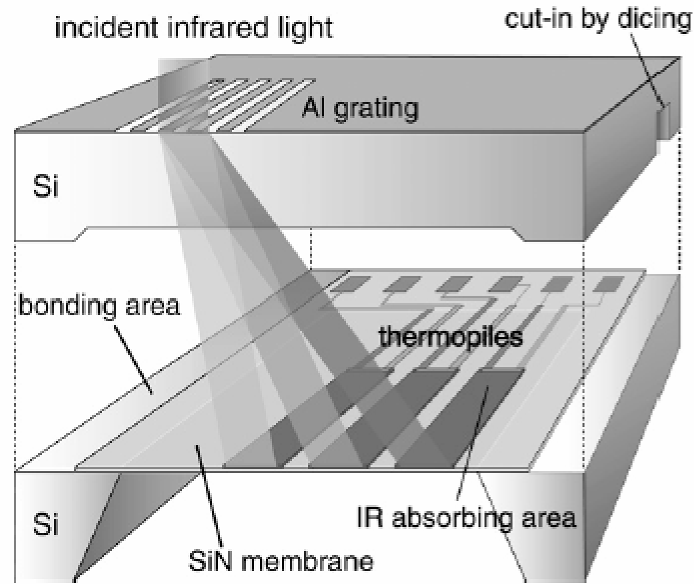

Fig. 1-13 A grating-based microspectrometer [13]

be bonded to form the microspectrometer.

In the above examples, few of them have combined the actuators and optical sensors in one integrated process. Through the proposed spot profile measurement system, we will demonstrate the integration of the MEMS actuator, photo detector, and circuit on a single chip.

1.5.3 Devices in CMOS MEMS

CMOS MEMS is a technology to integrate the circuits with MEMS structures using the standard CMOS process. For the absorption type knife edge scanning device, a fully integrated system including circuits is an important target to handle complex signal processing in real-time.

In resent researches, integrated comb drives have been widely used for electrostatic actuation, capacitive position sensing and frequency tuning. They have become a part of many MEMS devices such as accelerometers [14], gyroscopes [15], and microscanners [16]. A released gyroscope fabricated by the thin-film CMOS-MEMS process is shown in Fig. 1-14. It includes a z-axis comb drive, a

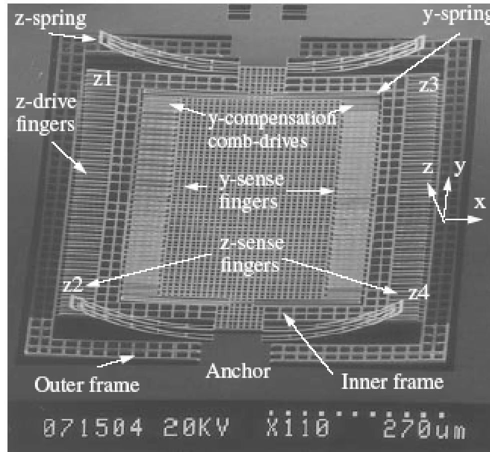

Fig. 1-14 A lateral-axis gyroscope [16]

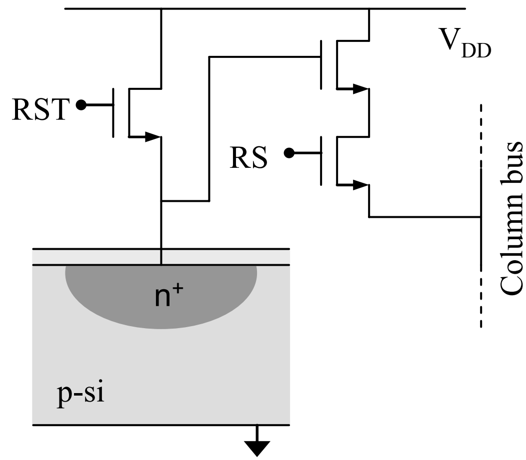

Fig. 1-15 A APS pixel [17]

y-axis accelerometer and a z-axis position sensor. The inner frame (proof mass) is driven to vibrate in the z-direction by the comb drive while the induced Coriolis acceleration is sensed. CMOS active pixel sensors (APS), fabricated using a standard CMOS process, have advantages of low cost, low power consumption and high levels of integration [17]. Due to intensive works for past several years, CMOS APS imagers are now considered as an alternative to CCDs in many application fields. A p-n junction is used to form a photodiode. By addressing (row-select, RS) and resetting (RST) the pixel (Fig. 1-15), the optical signal is sensed and fed to the column to construct the image.

From the above survey, both the comb actuator and optical sensor can be fabricated by CMOS and its post process. Thus, the CMOS MEMS device is considered feasible to integrate all the mentioned electro-optical components and even signal processing circuits in a single chip.

1.6 Objectives and thesis organization

The objective of the thesis is to develop a micro optical spot profile measurement system based on the scanning knife-edge method. An absorption type device will be

fabricated to measure the spot profile whereas a reflection type device is used as reference. Both prototypes are fabricated using SOI processes. A CMOS MEMS device with the TSMC 0.35 μm 2P4M process will be developed to demonstrate the integration of photo detector, comb actuator, and circuits in a single chip.

In this thesis, the design and analysis will be given in Chapter 2. The fabrication technology is discussed in Chapter 3. Preliminary experimental results of such a MEMS optical spot profile measurement system are presented in Chapter 4. Finally, conclusion and future work are discussed in Chapter 5.

Chapter 2 Design and Analysis

In the MEMS-based spot profile measurement system, the scanning knife-edge plate is actuated by a comb actuator and the optical distribution is detected by a photo detector. To construct the measurement system, the design and analysis of such a comb drive actuator and photo detector are discussed in this chapter. Both the SOI and CMOS devices are included for their easier implementation and possibility of integration with circuits, respectively.

2.1 Comb drive actuator

A folded flexure comb drive actuator is analyzed by the finite element modeling (FEM) for the static and dynamic characteristics. The suspended comb is actuated by the voltage applied between fixed and movable combs. After the desired displacement is determined, the comb can be designed from the balance of the spring force and the electrostatic force.

2.1.1 Spring constant

For a spring element with pure bending and bonding constraints as shown in Fig. 2-1 (a), the spring constant k_x in x-direction is [18]:

$$k_x = \frac{F_x}{x} = \frac{Ehb^3}{L^3}, \tag{4}$$

where F_x is the force in the x direction, x is the relative displacement of the movable end of the spring, E is Young's modulus, h is the spring thickness, b is the width of he spring and L is the length of the spring.

In order to reduce device layout area and provide large deflection, a folded flexure structure is usually used (Fig. 2-1 (b)). In this structure, the spring constant

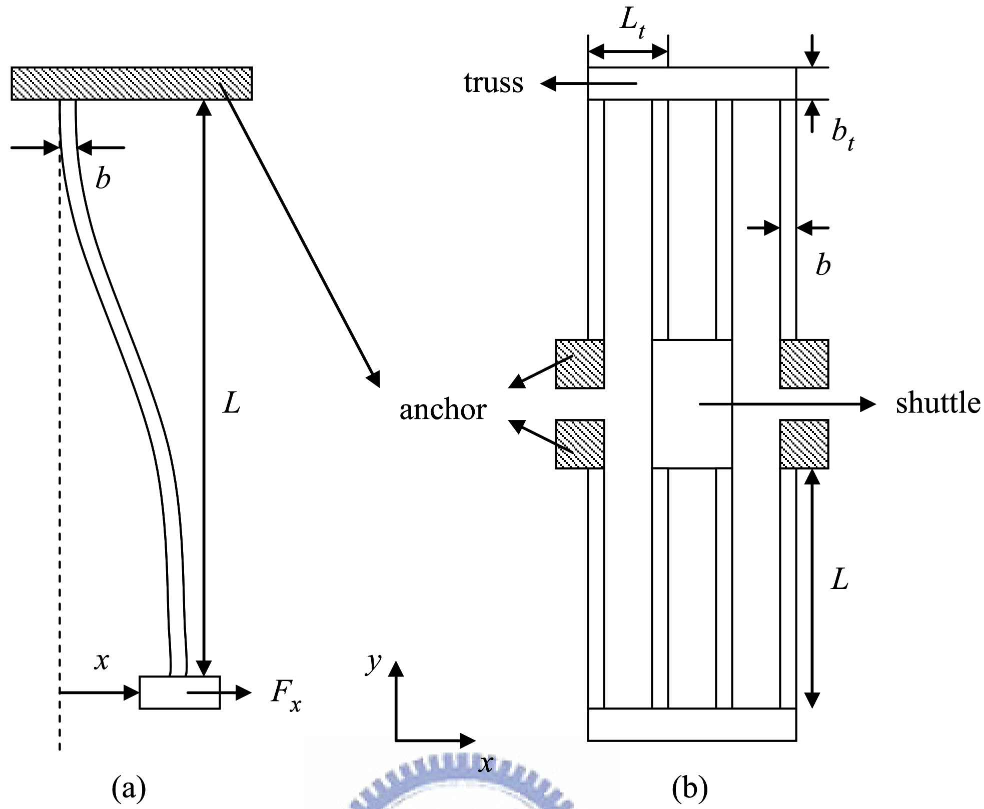

Fig. 2-1 (a) A sprig element (b) folded flexure structure

cab be calculated from [19]:

$$k_x = \frac{2Ehb^3}{L^3} \frac{L_t^2 + 14\alpha L_t L + 36\alpha^2 L^2}{4L_t^2 + 41\alpha L_t L + 36\alpha^2 L^2}, \tag{5}$$

where b_t is the width of truss beam, L_t is the length of truss beam and $\alpha = (b_t / b)^3$.

2.1.2 Comb drive actuator

In the lateral driven comb actuator, a movable part (rotor) and a stationary part (stator) of comb fingers are engaged. One cell of the comb is shown in Fig. 2-2. To simplify the electrostatic analysis, the combs are approximated by a parallel plate model. Therefore, 3D effects like fringing fields, comb-finger end effects and the ground-plane levitation effects are neglected [20].

The capacitance between the stator and rotor can be expressed as:

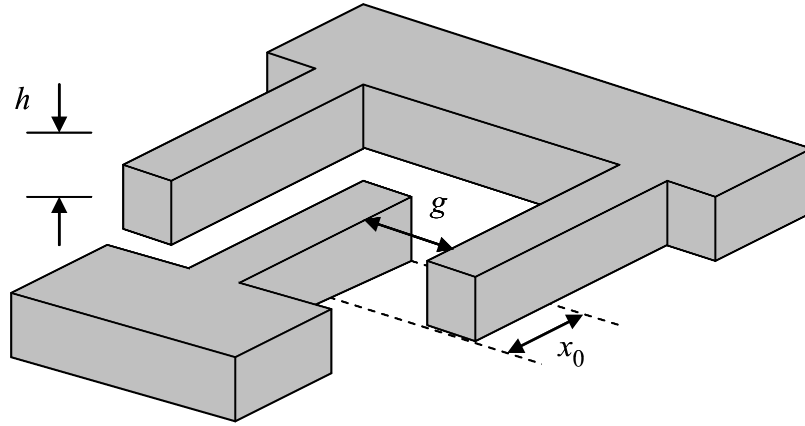

Fig. 2-2 Cell of engaged comb drive arrays

$$C = \frac{2n\varepsilon_0 h\left(x + x_0\right)}{g}, \tag{6}$$

where n is the number of fingers of one side, ε_0 is the dielectric constant of air, which is 8.85×10^{-12} F/m, h is the thickness of fingers, x_0 is the initial finger overlap, x is the comb finger lateral displacement and g is the gap spacing between the fingers. The lateral electrostatic force in the x-direction for a constant applied voltage V is equal to the derivative of the electrostatic energy with respect to x:

$$F_x = \frac{1}{2}\frac{\partial C}{\partial x}V^2 = \frac{n\varepsilon_0 h}{g}V^2 \tag{7}$$

According to Eq. (7), to obtain a large force while keeping a relative low applied voltage, finger number n should be large and the gap g should be small.

Additionally, there is an elastic force of the suspened beam along x-direction to pull the movable fingers back. When the net electrostatic force and the spring elastic force are equal, the displacement d can be expressed as [21]:

$$F_s = k_x d = F_x \;\Rightarrow\; d = \frac{n\varepsilon_0 h}{g k_x}V^2, \tag{8}$$

where F_s is the elastic spring force in the x-direction. From Eq. (8), it can be seen that decreasing the comb gap g and increasing the electrostatic voltage will increase the static displacement.

2.1.3 Resonant frequency

The actuator is to be operated in the lateral resonance mode. At the resonance frequency, the comb actuator can be driven to a larger displacement with a smaller applied voltage. The resonant frequency can be obtained from Rayleigh's quotient [22]. The expression for the fundamental resonance frequency f_0 is:

$$f_0 = \frac{1}{2\pi}\sqrt{\frac{k_x}{M_{shuttle} + \frac{1}{2}M_{truss} + \frac{96}{35}M_{spring}}}, \tag{9}$$

where the denominator of the fraction in the square root is the equivalent mass with $M_{shuttle}$ being the mass of the shuttle, M_{truss} the mass of the single truss and M_{spring} the mass of a single spring. The resonant frequency is ideally independent of the driving voltage.

2.1.4 Geometric design of SOI device

In the SOI device, a folded flexure comb actuator is used. All the springs have equal length. The whole layout is schematically shown in Fig. 2-3. The line width is constrained by the capability of photolithography. Therefore, the finger width and the gap spacing are 4 μm. The width of the spring is about twice the line width for the fabrication tolerance of the metal line on top. The device thickness is 20 μm. The truss width (25 μm) is larger than the spring width (10 μm) so that the full truss structure can be viewed as rigid body.

To measure the spot profile correctly, the scanning range should be large enough to cover the entire spot width. If the maximum spot size to be measured is about 5 μm, a scanning range of ±10 μm at resonance can be determined from twice of the spot size. The actuator design is then discussed in the following.

With a typical Q = 100 [23], a static displacement amplitude of 0.1 μm is need. Assume the applied voltage is limited to 30 volts, the finger number can be calculated

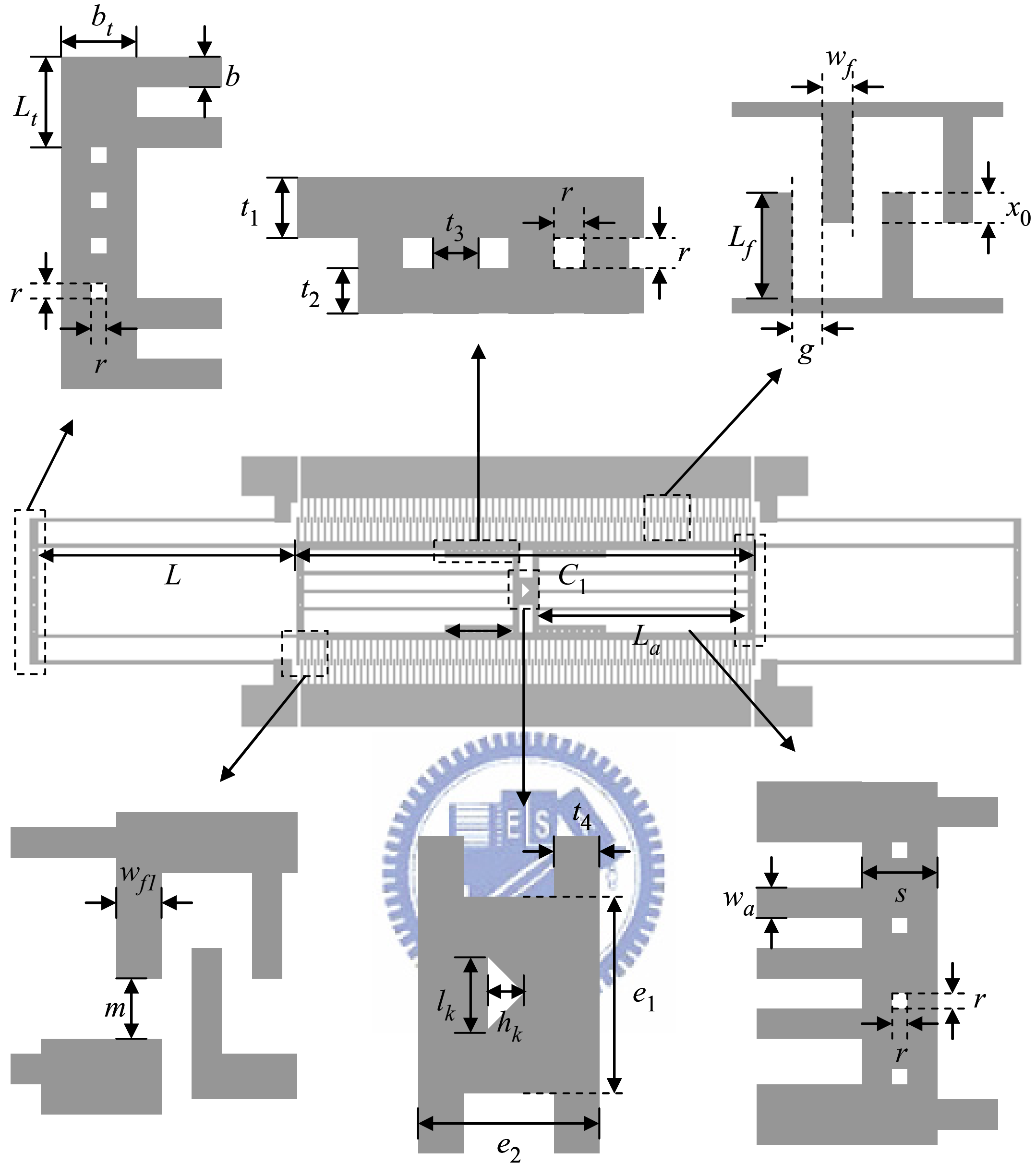

Fig. 2-3 SOI comb actuator layout

by Eq. (8). To achieve a larger deflection, a long spring length of 680 μm is used to reduce the spring constant. An overlap x_0 of 15 μm, which is larger than the resonant amplitude, is used to provide an initial electrostatic force. The last finger in the movable comb has a larger width of 8 μm to counter the unbalance electrostatic force. The detail geometric parameters are listed in Table 2-1. With a spring constant k_x =15.3 N/m and proof mass M =6.6×10^{-9} kg, a static displacement of 0.1 μm can be achieved with finger number n of 70.

Since the system should be operated in the lateral resonance mode, measurement error will occur if other modes, such as the vertical or torsional modes, are induced. Therefore, the nearest mode to the lateral mode should be 3 kHz apart at least. In a high-Q narrow-band resonant system, this mode separation is large enough to suppress other unwanted modes. CoventorWare is used to simulate the resonance frequency by the finite element method (FEM). After meshing and boundary condition setting, first six resonance frequencies are founded and listed in Table 2-2. Fig. 2-4 showed the first three simulated resonant mode. It can be seen that the first mode is the desired lateral mode with a resonant frequency of 7.31 kHz, which is close to the theoretical analysis (7.58 kHz) shown in Table 2-1.

Table 2-1 SOI comb actuator layout parameters

Parameter	Dimension	Unit	Parameter	Dimension	Unit
spring length L	680	μm	triangle base l_k	30	μm
spring width b	10	μm	triangle height h_k	15	μm
finger length L_f	60	μm	thick finger w_{f1}	8	μm
finger width w_f	4	μm	mechanical stop m	30	μm
overlap x_0	15	μm	release hole r	4	μm
gap spacing g	4	μm	thickness t	20	μm
truss length L_t	74	μm	density ρ	2.3	g/cm^3
truss width w_t	20	μm	proof mass M	6.6×10^{-9}	kg
shuttle length C_1	1110	μm	Young's modulus E	169	GPa
arm length L_a	508	μm	spring constant k_x	15.3	N/m
arm length w_a	10	μm	finger number n	70	
rectangle length e_1	100	μm	applied voltage V	30	volts
rectangle width e_2	60	μm	device area	1000×2500	μm^2
width t_1	20	μm	resonance freq. f_0	7.58	kHz
width t_2	15	μm	Quality factor	100	
width t_3	14	μm	static displacement amplitude @ 30V	0.1	μm
width t_4	14	μm			
width s	20	μm	total displacement	±10	μm

Table 2-2 Mode frequencies of SOI device by CoventorWare

mode	Frequency (Hz)	
1	7.32E03	→ lateral mode
2	1.24E04	→ vertical mode
3	2.43E04	→ tortional mode
4	2.84E04	
5	3.16E04	
6	1.29E04	

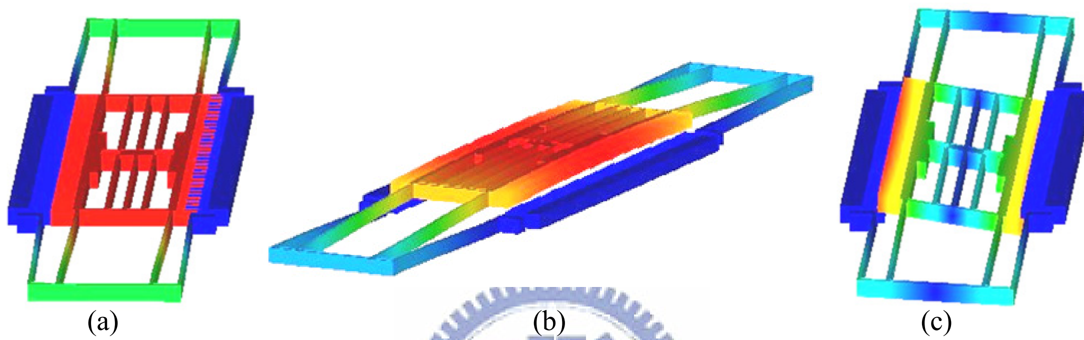

Fig. 2-4 Mode analysis of SOI comb actuator: (a) first (lateral), (b) second (vertical), (c) third (torsional)

1896

2.1.5 Geometric design of CMOS MEMS device

Using the CMOS MEMS process, a comb actuator with readout circuit can be achieved to scan the spot and analyze the signal on a single chip. The TSMC 2P4M 0.35 μm process (Fig. 2-5) consists of metal layers (aluminum), dielectric layers (SiO_2), via layers (tungsten) and the silicon substrate. In our CMOS comb design, tungsten is not used in order to reduce the spring constant. The composite comb structure layers (Fig. 2-6) is analyzed below.

The minimum line width is 2 μm, limited by the post fabrication capability. The device thickness is 5 μm, which is the sum of three metal layers and three dielectric layers (Table 2-3). A mesh structure is used in the actuator since the large rectangular opening can help undercut the silicon substrate. The whole layout view is shown

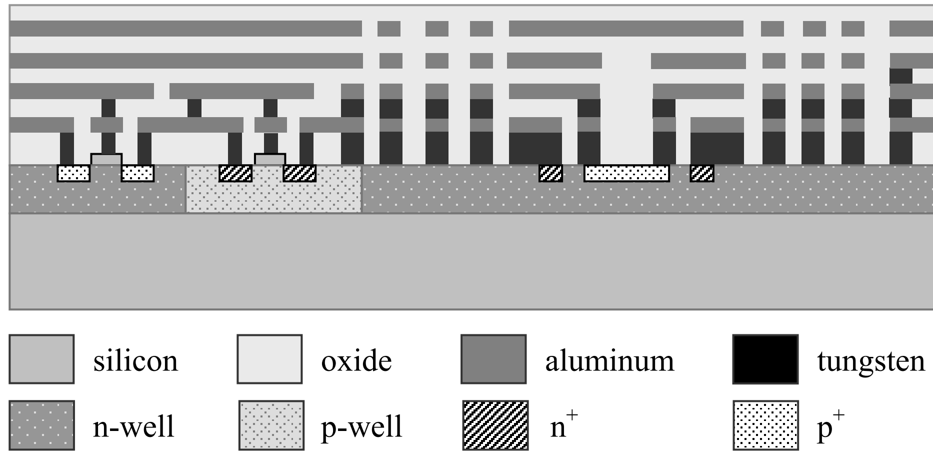

Fig. 2-5 Cross section view of TSMC 2P4M 0.35 μm process

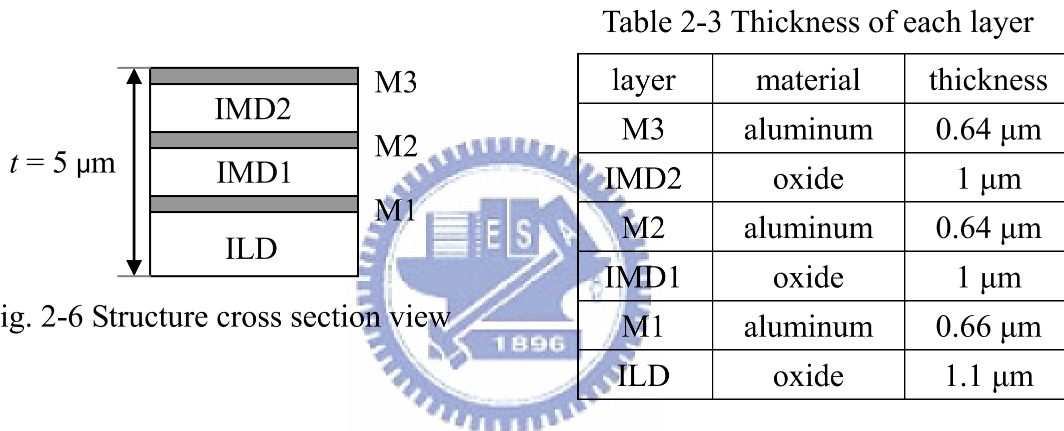

Fig. 2-6 Structure cross section view

Table 2-3 Thickness of each layer

layer	material	thickness
M3	aluminum	0.64 μm
IMD2	oxide	1 μm
M2	aluminum	0.64 μm
IMD1	oxide	1 μm
M1	aluminum	0.66 μm
ILD	oxide	1.1 μm

in Fig. 2-7.

Due to the uncertainty of the quality factor in CMOS-MEMS devices, a proper assumption of Q = 10 is used to calculate the geometric dimensions of the actuator. For a total displacement of ±10 μm, static displacement of 1 μm is needed. Because the dielectric films in the composite beam have no contributions to electrostatic force, the effective thickness of fingers is 1.94 μm, rather than the finger thickness (5 μm). Restricted by the CIC tapeout area limitation (2500x2500 μm^2), the shorter spring length L of 280 μm and fewer finger number n of 40 are used. Therefore, the applied voltage has to be increased to 60 volts to achieve the desired displacement. The layout area is 800x450 μm^2.

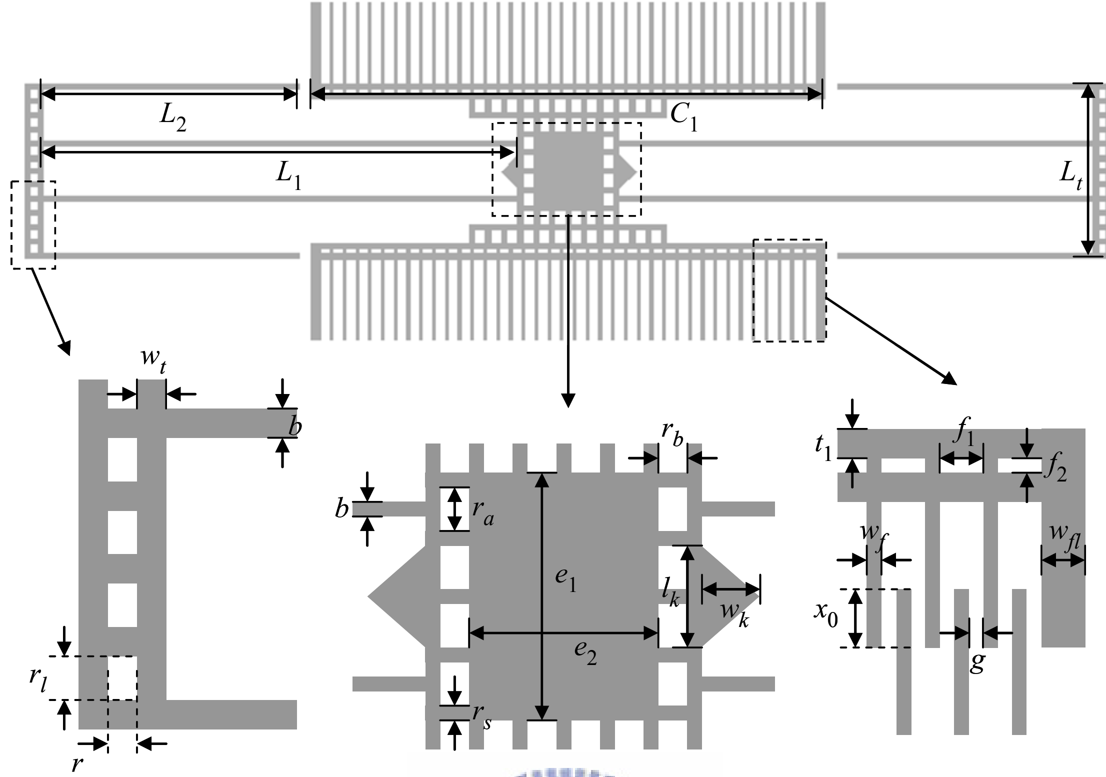

Fig. 2-7 CMOS comb actuator layout

In the composite material layers in the device, the equivalent Young's modulus E_{eff} is calculated by the following equation [24]:

$$E_{eff} I_{eff} = \sum_{j} E_j I_j , \tag{10}$$

where I_{eff} is the moment of inertia of the composite beam and I_j is the moment of inertia of the jth layer. I_{eff} and I_j can be evaluated according to the parallel theorem:

$$I_j = \frac{bh_j^3}{12} + A_j d_j^2 , \tag{11}$$

where b is the structure width, h_j is the thickness of film, A_j is the cross-sectional area ($A_j = bh_j$), and d_j is the distance between the centurial axis of the composite beam and the neutral axis of the jth film. The proof mass can be calculated as product of the equivalent density and the volume, where the equivalent density ρ_{eff} can be derived from:

$$\rho_{eff} t_{total} = \rho_{Al} t_{Al} + \rho_{oxide} t_{oxide}, \tag{12}$$

where t_{total} is the thickness of the composite beam, ρ_{Al} is the density of aluminum, ρ_{oxide} is the density of oxide, t_{Al} and t_{oxide} are the total thickness of aluminum and oxide layers, respectively.

Based on the above discussion, the calculation results of the spring constant k_x and the proof mass M are 1.65 N/m and $3.4\text{x}10^{-10}$, respectively. Therefore, the resonant frequency can be calculated to be equal to 12.1 kHz. To release the structure, opening holes sized from 4x4 μm^2 to 8x8 μm^2 are distributed on the device to help undercut the substrate. After the theoretical calculation, the detail parameters, including geometric dimension and mechanical properties, are listed in the Table 2-4.

Table 2-4 CMOS comb actuator layout parameters

Parameter	Dimension	Unit	Parameter	Dimension	Unit
spring length L_1	280	μm	triangle base l_k	20	μm
spring length L_2	150	μm	triangle height h_k	10	μm
spring width b	4	μm	thick finger w_{f1}	6	μm
finger length L_f	60	μm	width r_s	4	μm
finger width w_f	2	μm	width t_1	4	μm
overlap x_0	15	μm	thickness t	5	μm
gap spacing g	2	μm	density ρ	2.33	g/cm^3
truss length L_t	110	μm	proof mass M	$3.4\text{x}10^{-10}$	kg
truss width w_t	4	μm	Young's modulus E	70	GPa
shuttle length e_1	50	μm	spring constant k_x	1.65	N/m
shuttle width e_2	44	μm	finger number n	40	
release hole r_l	6	μm	applied voltage V	60	volts
release hole r	4	μm	device area	800x450	μm^2
release hole r_a	8	μm	resonance freq. f_0	12.1	kHz
release hole r_b	6	μm	Quality factor	10	
release hole f_1	5.5	μm	static displacement amplitude @ 60V	1	μm
release hole f_2	2.5	μm			
length C_1	322	μm	total displacement	±10	μm

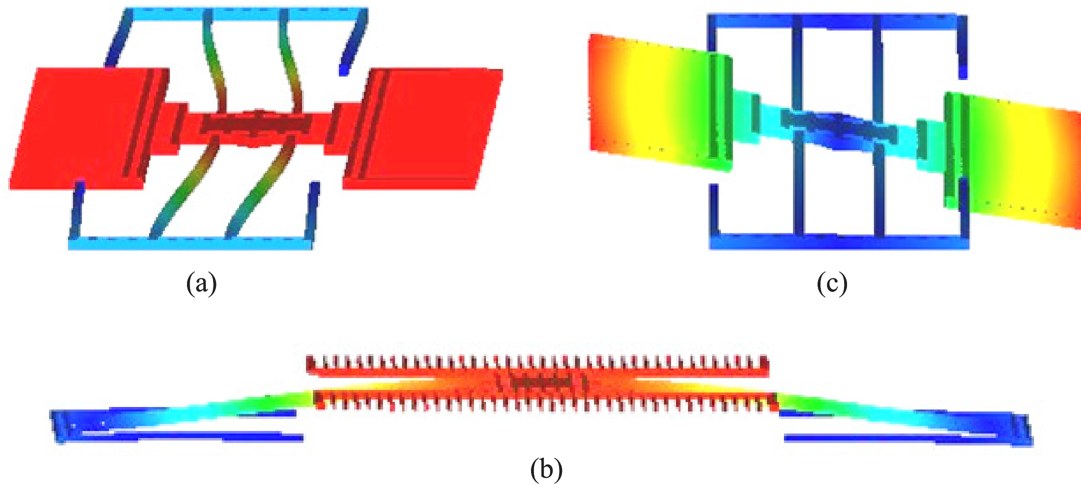

Fig. 2-8 Mode analysis of CMOS comb actuator: (a) first (lateral @ 12.9 kHz), (b) second (vertical @ 15.4 kHz), (c) third (torsional @ 22.4 kHz)

The modal simulation is shown in Fig. 2-8. The first mode (lateral mode) is 12.9 kHz, close to the theoretical value. The second mode is 15.4 kHz (vertical mode), apart from the first mode of only 2.5 kHz due to the thinner structure thickness (5 μm) in the CMOS process.

Despite of the precise fabrication service by CMOS foundries, the photolithography misalignments of the metal layers still exists (Fig. 2-8 (a)). The unbalanced residual stresses between each layer make the suspended structure cured laterally. In order to reduce this effect, the lower metal layers are made wider to tolerate the photolithography error [25]. As shown in Fig. 2-8 (b), a 0.1 μm width difference between metal-1, metal-2, and metal-3 is used for the comb fingers and springs.

At the same time, the large vertical stress gradients can result in an out-of-plane curling. As illustrated in Fig. 2-9 (a), curl mismatching of fingers significantly reduce the overlap. The decreased electrostatic force and sidewall capacitance make it hard for actuating and sensing. To solve the problem, fingers on the stator side are attached to a rigid frame [26]. The rigid frame is anchored along a common axis with the proof

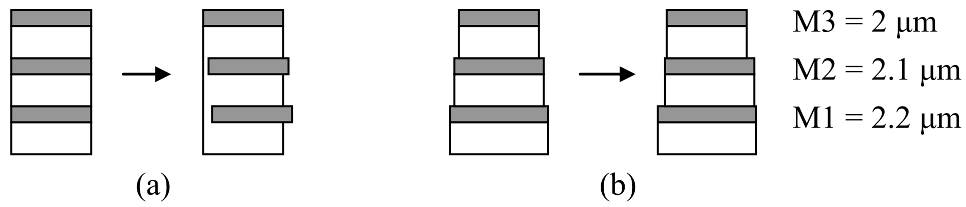

Fig. 2-9 Cross section view of a: (a) normal beam (b) improved beam

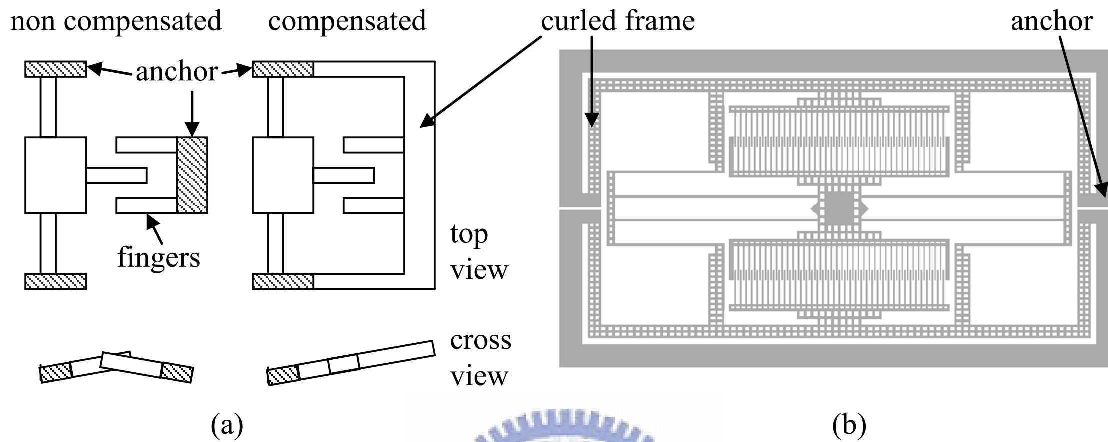

Fig. 2-10 (a) Compensation of fingers (b) top view of the full layout

mass, and is subject to the same stress gradient as the inner structure. Thus, the curl matching can be achieved. To get optimal matching, the frame consists of 4 μm width and release holes of 4×4 μm^2. For the symmetry of compensation, the area of the single CMOS device, including the rigid frame, is 800×450 μm^2.

2.2 Photo detector

The silicon photodiodes have been widely used as standard photo detectors for the light wavelength ranged from 100 nm to 1100 nm. In the absorption-type spot profile measurement system in the SOI substrate, a p-n junction photodiode is fabricated by ions implantation to detect the optical intensity. A theoretical analysis of detector characteristics is presented in the following.

2.2.1 Silicon photo detector

A silicon photo detector has a depletion layer with a built-in electric field to separate photogenerated electron-hole pairs. Consider a photo detector with a depletion region of thickness of W in a p-type silicon substrate. The photocurrent i arising from the effective incident optical power P_{in} is related to the responsivity ρ. Assume the substrate is the dominant source of diffusive transport, and neglecting other sources of minority carriers in the substrate, the photocurrent i and responsivity ρ can be derived from [27]

$$i = P_{in}\rho, \tag{13}$$

$$\rho = \frac{\eta q}{h\nu}(1-R)\left(\frac{1-e^{-\alpha W}}{1+\alpha L_n}\right), \tag{14}$$

$$L_n = \sqrt{D_n \tau_n}, \tag{15}$$

where α is the absorption coefficient, $1 - e^{-\alpha W}$ is the fraction of light absorbed in the depletion width W of the detecting junction, R is the reflection coefficient, L_n is the minority carrier diffusion length for electrons in the p-type substrate, q is the electron charge, $h\nu$ is the photon energy, and η is the internal quantum efficiency (the fraction of absorbed photons that give rise to collected electron-hole pairs). D_n and τ_n are the diffusion constant and minority carrier lifetime.

Better responsivity can be reached by enlarging the depletion width W. The depletion region width W can be calculated from [28],

$$W = \sqrt{\frac{2\varepsilon_0 (V_0 + V_b)}{qN_s}}, \tag{16}$$

where N_s is the substrate concentration, V_b is the bias voltage applied to the diode, and V_0 is the built-in voltage:

$$V_0 = \frac{kT}{q} \times \ln\left(\frac{N_s N_d}{2.25 \times 10^{25}}\right), \tag{17}$$

Fig. 2-11 A p-n junction photodiode: (a) cross section view (b) top view

where k is the Boltzmen constant, T is the absolute temperature and N_d is the doping concentration. From the above equations, low substrate concentration N_s and heavy doping N_d can be employed to increase the responsivity.

The schematic cross section view and the top view of photodiodes for the absorption type device are illustrated in Fig. 2-10. The n^+ region is used to form the p-n junction between the bottom of the n^+ and the p substrate. The outside p^+ region is used to form the ohmic contact to the p substrate. The width of the p^+ ring electrode is 3 μm and the size of the n^+ detector region is 36 μm ×18 μm. For the absorption type device, the conduction layer is patterned as a triangular shape on top of the n^+ region to form a knife-edge detection area. Under a proper reverse bias, a better sensitivity can be obtained. The photocurrent is transferred by conduction wire for further signal processing.

2.2.2 Responsivity

To obtain a high responsivity, arsenic (As) n^+ implantation is carried out with energy of 60 KeV and dose of 3×10^{15} cm^{-2}. A p-type wafer with a resistivity ρ = 10 ohm cm is used for the p substrate. The doping profile (Fig. 2-11) in the substrate is a Gaussian distribution given by [29]

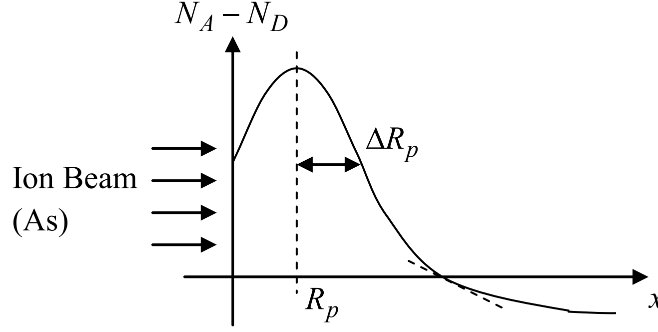

Fig. 2-12 Doping profiles of p-n junction

$$n(x) = \frac{\phi}{\sqrt{2\pi}\Delta R_p} \exp\left[-\left(\frac{x - R_p}{\sqrt{2\pi}\Delta R_p} \right)^2 \right], \tag{18}$$

where ϕ is the total numbers of ions per area, R_p is the projected range, ΔR_p is the projected straggle. From [30], the R_p and the ΔR_p can be found to be 0.035 μm and 0.015 μm, respectively. The peak concentration is 8×10^{20} ions/cm^3. By Eq. (18), the n^+ junction depth is found to be 0.15 μm at a substrate doping concentration of 1×10^{17} cm^{-3}. The light power P_{in} in the substrate is given by

$$P_{in}(x) = P_{inc} e^{-\alpha x}, \tag{19}$$

where P_{inc} is the incident photons flux at the surface and α is the absorption coefficient of silicon. For the red laser (λ=633nm) and the green laser (λ=543nm), α is 5000 cm^{-1} and 9500 cm^{-1}, respectively. The effective incident power P_{in} is 0.92 P_{inc} and 0.87 P_{inc}, respectively.

Under zero bias voltage (V_b = 0), the built-in voltage is 0.75 volts and the depletion width W is calculated to be 0.3 μm by Eq. (16). The minority carrier diffusion length is about 4 μm [31]. The reflection coefficient R of silicon is 0.35. From Eq (14), the responsivity at 633 nm and 543 nm wavelengths under a bias voltage from 0 to 15 volts are plotted and shown in Fig. 2-12. With the applied bias voltage increased, larger responsivity will be achieved. From the calculation, the

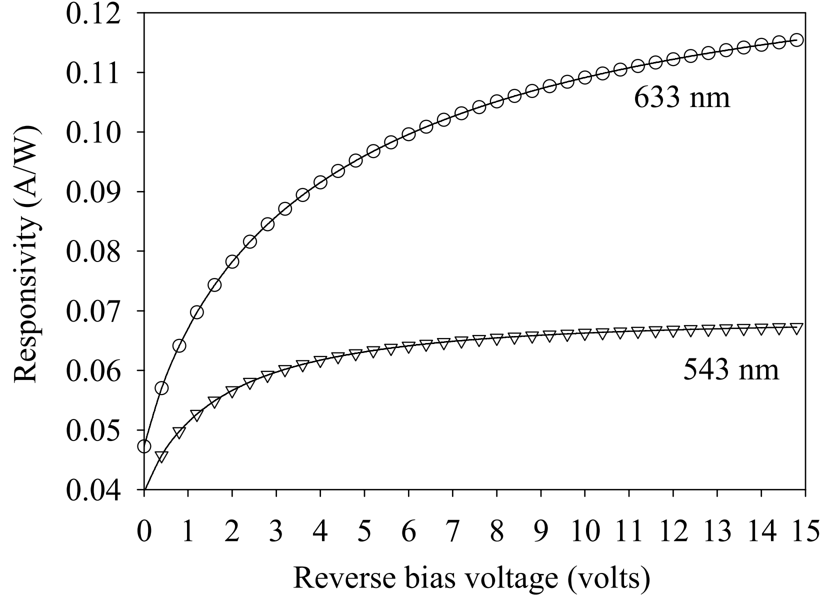

Fig. 2-13 Responsivity under reverse bias voltage

maximum possible responsivity of the red and green He-Ne lasers at a reverse bias voltage of 5 volts is 0.092 A/W and 0.063 A/W, respectively.

2.3 Signal analysis of spot profile measurement

The focused spot profile can be derived from the measured photocurrent waveform. From Eq. (8), the displacement of the comb is proportional to $V^2(t)$. Assume the applied voltage $V(t)$ is

$$V(t) = V_{DC} + V_{AC}\sin(\omega_0 t), \tag{20}$$

where the ω_0 is the resonance frequency. Then the corresponding dynamic equation can be expressed as:

$$\begin{aligned} m\ddot{x} + b_e\dot{x} + k_x x = F_e &= \frac{n\varepsilon_0 h}{g}\left(V_{DC} + V_{AC}\sin(\omega_0 t)\right)^2 \\ &= \frac{n\varepsilon_0 h}{g}\left[\left(V_{DC}^2 + \frac{V_{AC}^2}{2}\right) + 2V_{DC}V_{AC}\sin(\omega_0 t) - \frac{V_{AC}^2\cos(2\omega_0 t)}{2}\right] \end{aligned} \tag{21}$$

Therefore, there is a second harmonic component in the driving voltage. However, the

displacement response at this high frequency is much smaller than the peak resonance displacement. So the vibration is mainly caused by the fundamental component at the resonant frequency with a 90° phase shift. As showed in Fig. 2-13, the amplitude A_{ω_0} under the applied voltage at ω_0 is $2\frac{n\varepsilon_0 h}{gk_x}V_{DC}V_{AC}Q$, where Q is the quality factor.

As for the spot profile, a focused light spot can usually be approximated by a Gaussian distribution. The photocurrent is proportional to the integration of the power distribution over the detector surface. For the full width half maximum (FWHM)

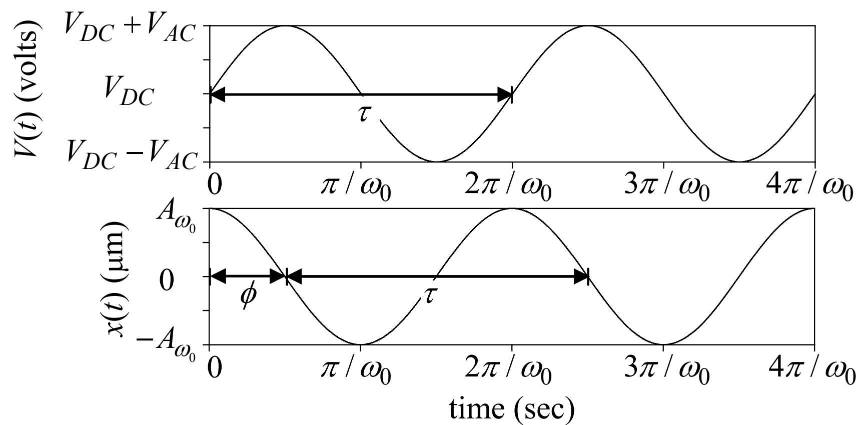

Fig. 2-14 Driving signal $V(t)$ and derived displacement $x(t)$

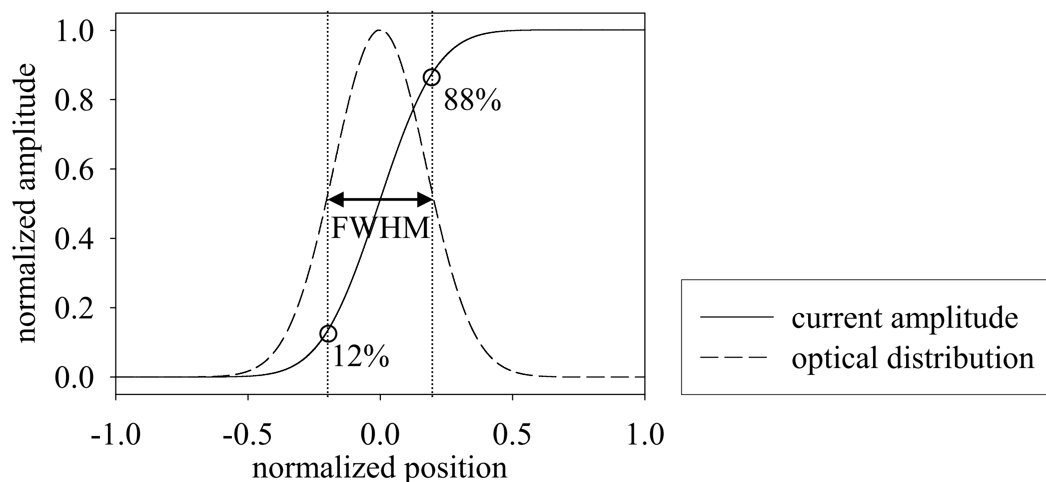

Fig. 2-15 Definition of FWHM in power and photocurrent distribution

definition, the optical spot size can be acquired from the photocurrent distribution between the 12% and 88% of its full scale, as shown in Fig. 2-15.

From the above discussions, the full signal processing from driving voltage to the measured optical distribution can be described as follows. First, a DC voltage V_{DC} and sinusoidal V_{AC} amplitude at resonant frequency are applied to the comb to actuate the plate. Then the signal detected by the built-in photodiode or the remote detector in a reflection type device is acquired. Two orthogonal directions (*x* edge and *y* edge) are measured in positive and negative scan of one cycle (Fig. 2-16 (a)). From the normalized photocurrent, four optical power distributions are measured in one scan period (Fig. 2-16 (b) (c)). However, the definition of FWHM is the optical

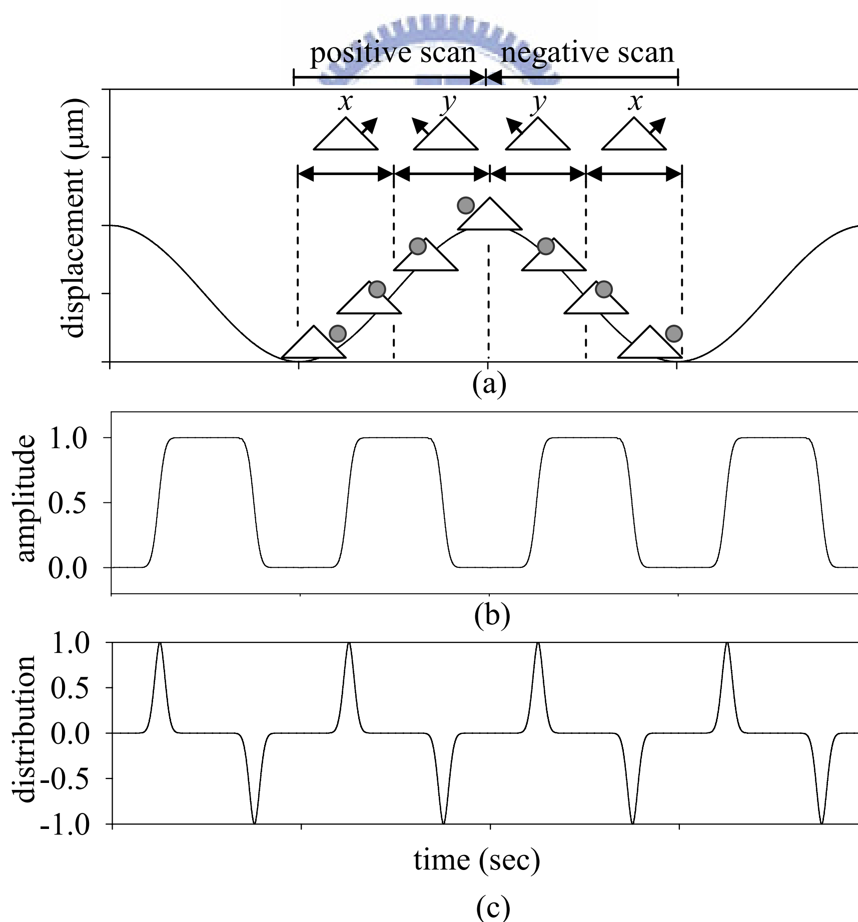

Fig. 2-16 Signal processing (a) displacement of knife edge plate (b) normalized current amplitude (c) normalized optical power distribution

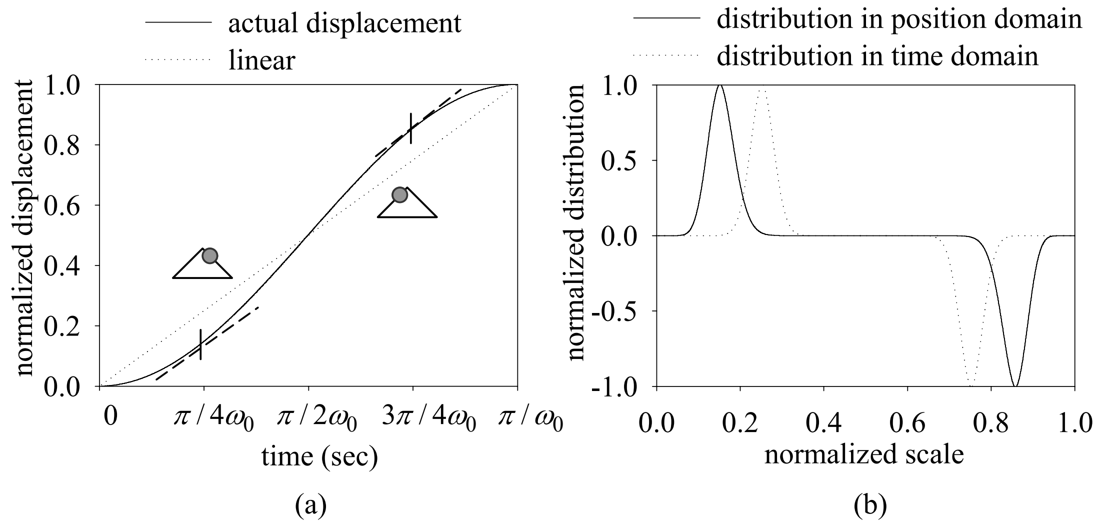

Fig. 2-17 (a) Actual displacement with time (b) normalized optical distribution in position domain and time domain

distribution based on the knife edge position instead of time. The knife edge position is proportional to the displacement but not linear to the driving voltage, as shown in Fig. 2-17 (a). The precise spot size can only be calculated at the normalized position. Therefore, the distribution in time domain t is then converted to the position domain x by:

$$x = 1 + \sin(\omega_0 t - \frac{\pi}{2}), \tag{22}$$

where $t = 0$ is the start point of the positive scan (Fig. 2-16(a)). Compared to the distribution in time domain, the focused spot distribution in position domain is detected earlier (Fig. 2-17 (b)) because the end of the vibration has a slower movement. At the same time, optical distribution of focused spot is found no obvious variances between the two domains due its similar scanning speed. Then the FWHM of the micro spot can be calculated with the normalized position. The actual measurement will be presented in Chapter 4

2.4 Conclusion

In this chapter, the theoretical analysis of the comb actuator, photo detector, and scanning knife edge system are presented. A high aspect ratio SOI comb and a CMOS thin-films comb are designed for large displacement and simulated by CoventorWare. Design parameters are found and the specifications are close to the simulation results. In the absorption type, a p-n junction photodiode is used to detect the optical distribution. Diode characteristics and the responsivitiy for different wavelengths (633 nm and 543 nm) are calculated. The operation of the measurement system is discussed and the relation between measured photocurrent and spot size are derived.

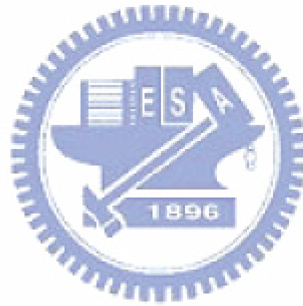

Chapter 3 Fabrication

The details of the fabrication in the SOI process and post CMOS process are presented. The SOI device was successfully fabricated in the third run, while the first two runs suffered from the problems of release and residual stresses. CMOS and post CMOS processes are also discussed. A series of test experiments were performed for the post process to verify the feasibility.

3.1 SOI process

SOI MEMS process is a convenient way to fabricate suspended structures. Some of the difficulties in MEMS fabrication such as isolation, high aspect ratio, and flat etched surface profile can be overcome more easily by using a SOI wafer.

For the absorption type device, a photo detector and a comb actuator need to be fabricated using the same process. With the capability of fabrication taken into consideration, the process steps are shown in Fig. 3-1. A thin Si_3N_4 film was deposited by LPCVD on the n-type <100> SOI wafer to isolate the electric signals (Fig. 3-1 (a)). The nitride was etched by RIE to form the mask for the following doping process (Fig. 3-1 (b)). Boron (B) ion implantation was then performed to form p^+ region of the photodiode in the n substrate; arsenic (As) ion implantation was used for ohmic contact to the n substrate (Fig. 3-1 (c)). The implanted ions were activated after each doping step by annealing. For driving and sensing, an aluminum layer was coated and patterned by RIE (Fig. 3-1 (d) (e)). At the same time, a triangular open region in the p^+ region was defined by the metal layer to serve as the knife-edge detection area. For the 20 μm etch of silicon by inductively coupled plasma (ICP), the photoresist mask was coated thicker to avoid the over etch of the photoresist caused by the bad

selectivity between silicon and photoresist. Then the comb structure was defined and the photoresist above was preserved to protect the aluminum from the wet etching at the subsequent release step (Fig. 3-1 (f)). Finally, the sacrificial layer (SiO_2) was removed by BOE (Fig. 3-1 (g)). After photoresist removing, sample cleaning, and IPA rinsing, the device was released by CO_2 drying (Fig. 3-1 (h)). The released device was wired to the PCB board to be tested and measured. The detail of process parameters are shown in Table 3-1.

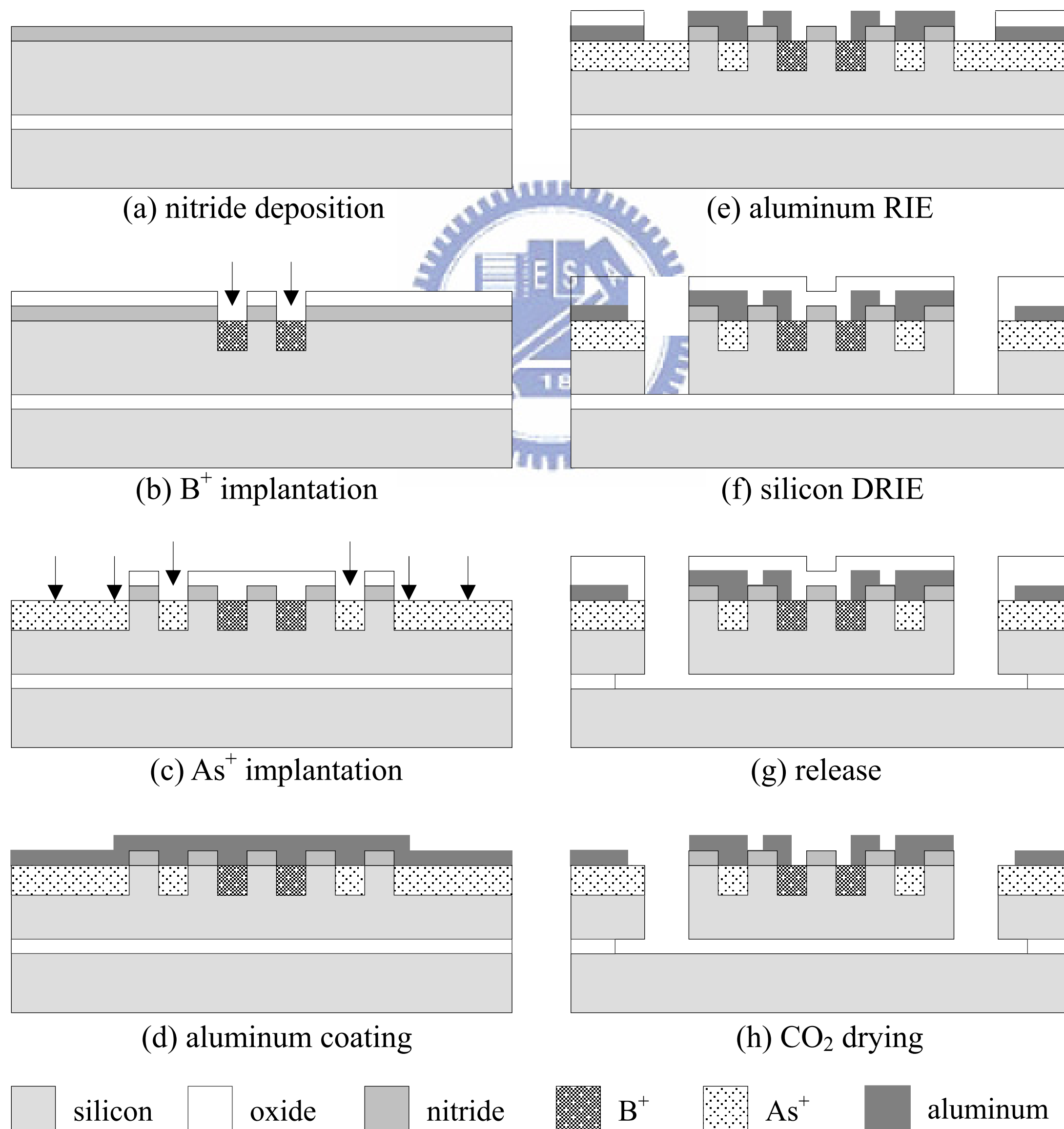

Fig. 3-1 SOI fabrication process

Table 3-1 Detailed SOI fabrication process

step	action	parameter	thickness/depth	place
1	RCA clean			
2	LPCVD Si_3N_4	800°C, 180 mTorr SiH_2Cl_2/NH_3=105:35	3500 Å	SRC
3	1st photolithography	FH6400 exposure 30s with filter	0.8 μm	SRC
4	RIE Si_3N_4	50 mTorr, 100W $SF_6:CHF_3$=30:10	3500 Å	SRC
5	B ion implantation	dose $3\times10^{15}/cm^2$, 30KeV		NDL
6	activate with RTA	900°C, 10s		SRC
7	remove photoresist	O_2 plasma 5 min		SRC
8	2nd photolithography	FH6400 exposure 30s with filter	0.8 μm	SRC
9	RIE Si_3N_4	50 mTorr, 100W $SF_6:CHF_3$=30:10	3500 Å	SRC
10	As ion implantation	dose $3\times10^{15}/cm^2$, 60KeV		NDL
11	activate with RTA	900°C, 15s		SRC
12	remove photoesist	O_2 plasma 5 min		SRC
13	metallization	thermal coat aluminum	5000 Å	SRC
14	3rd photolithography	FH6400 exposure 30s with filter	0.8 μm	SRC
15	RIE Al	10 mTorr, 120W $BCl_3:Cl_2$=40:40	5000 Å	SRC
16	remove photoresist	O_2 plasma 5 min		SRC
17	4th photolithography	FH6400 1st spin 500 rpm 2nd spin 1500 rpm soft bake 3 min exposure 45s with filter post bake 20 min	2 μm	SRC
18	ICP silicon	operated by CSUN	20 μm	CSUN
19	dicing			
20	release	BOE 40 min	1 μm	SRC
21	remove photoresist	ACE 30 min		SRC
22	CO_2 drying	cooling to 4°C		MOEMS lab (SRC)

3.2 Fabrication problems in the SOI process

During the fabrication process of the SOI device, the encountered problems and their solutions are discussed in this section.

3.2.1 Al protection

The process steps of the first run were mentioned in last section. The first problem occurred at the release step. The chemical solutions for oxide etching can also etch aluminum. Although the photoresist can protect the metal line from being exposed to the solution, the long etching time of oxide resulted in the peel off of the photoresist film. Therefore, several oxide etching solutions, such as BOE, SILOX VAPOR III enchants, concentrated HF, and the mixtures of HF and H_2O in different ratios were tried. However, These experiments showed similar results. Vapour etching using the above solutions was thus considered because the peel-off of photoresist can be greatly reduced in phase. At the last, condensed HF vapour etching was found to have the best selectivity between oxide and aluminum. However, vapour HF etching for 12 minutes was still too long; some the fewer aluminum wires were etched (Fig. 3-2 (a)) and peeled off of metal film was observed (Fig. 3-2

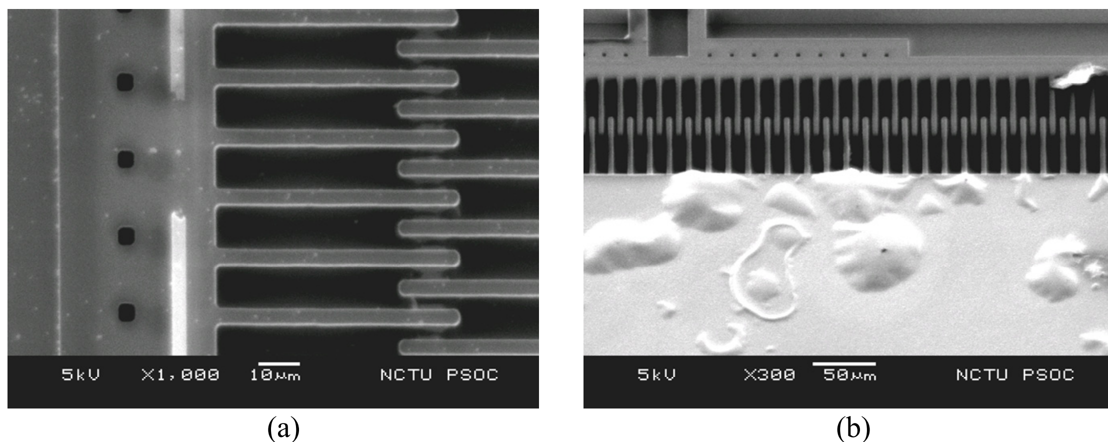

(a) (b)

Fig. 3-2 SEM (a) etched aluminum wire (b) peeled off aluminum film

(b)). A shorter release time was needed. Therefore, the thickness of the sacrificial layer was increased from 1 μm to 2 μm to reduce the release time. Since a better photo detector reponsivity can be achieved by large depletion region, the second fabrication run began with a p-type SOI wafer with a 2 μm thick oxide layer and higher resistivity (10 Ω/cm). The sequence of As and B ion implantations was exchanged to keep the lighter ions (B) from overtime annealing. The other processes were unchanged.

3.2.2 Stresses effect

A thicker oxide decreased the release time indeed and the metal lines were mostly preserved after the release. Compared with the first run, the undercut etching rate of 50 Å/sec is raised to 320 Å/sec with condensed HF vapour etching. But another problem appeared. The fabricated device was stuck to the substrate after CO_2 drying. From a WYKO interferometer measurement, the curling of long spring

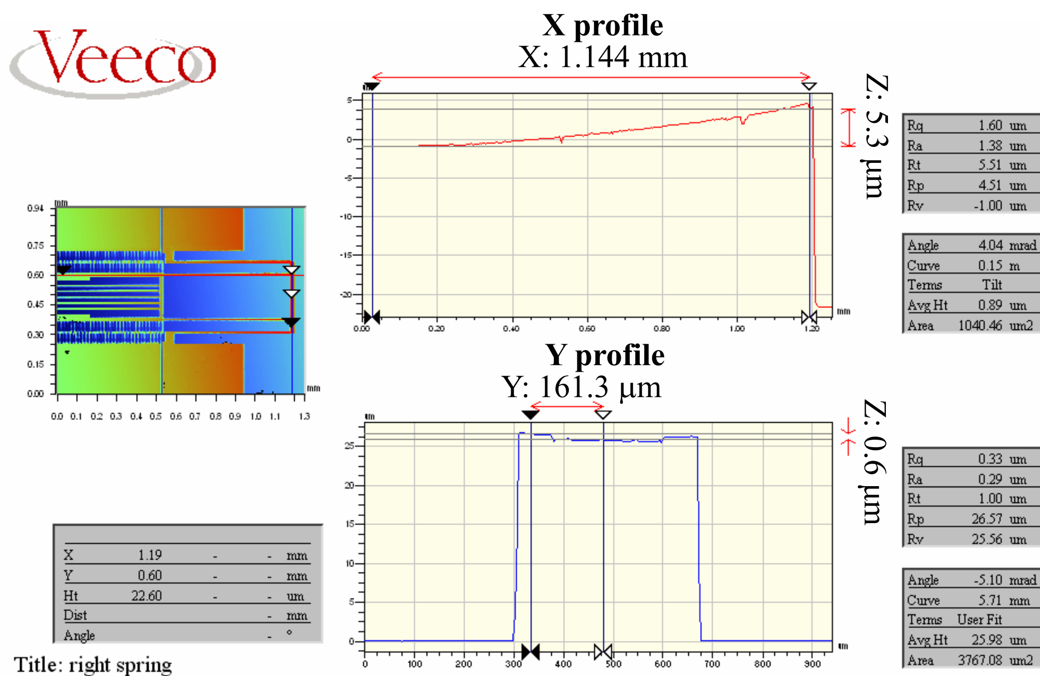

Fig. 3-3 Curling by residual stresses in SOI device

beams was observed (Fig 3-3). The stressed structure of the spring beam is illustrated in Fig. 3-4. The downward deflection of the centre part resulted in the stiction to the substrate. It is believed the residual stress of the nitride film on the suspended silicon is the main reason while the aluminum layer on top of the nitride may also contribute to the deflection. Although the large thickness of silicon (20 μm) greatly reduced the residual stress effect, the deflection about 3.3 μm of the 1300 μm long beam was still large than the thickness of sacrificial layer of 2 μm.

SEM results of the curled device were shown below. A larger gap between substrate was observed at the truss of the device (Fig. 3-4 (a)). An obviously tilt at the tip of a broken beam was also found as shown in Fig. 3-4 (a). At the same time, the

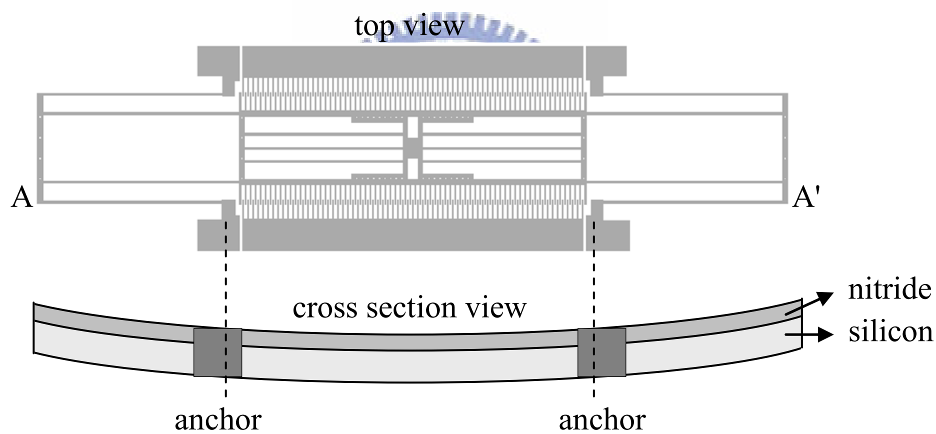

Fig. 3-4 Top view and AA' cross section view of the stressed structure

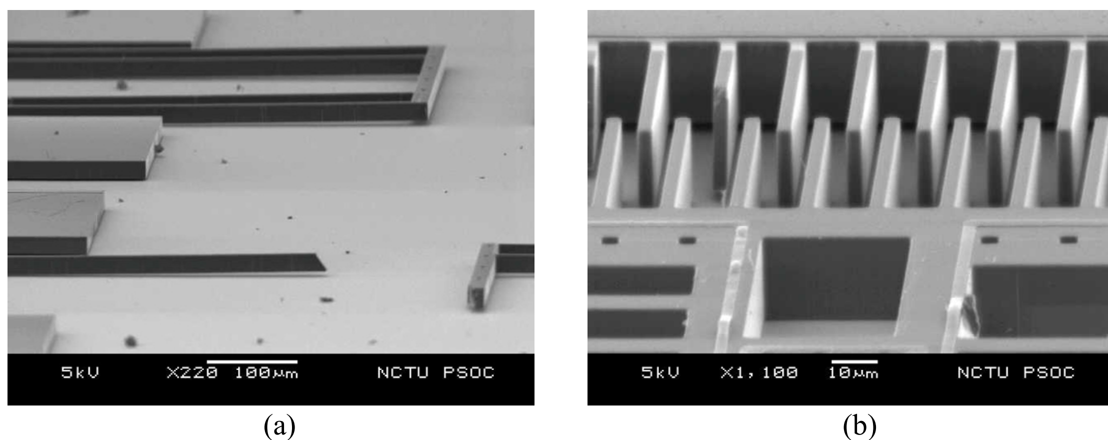

(a) (b)

Fig. 3-5 SEM of (a) deflected beams (d) structure stuck on the substrate

centre part of the structure was stuck on the substrate (Fig. 3-4 (b)).

3.2.3 Backside etching

To reduce the deflection caused by the residual stresses, a thinner low-stress LPCVD Si_3N_4 film could be used while the other variables, such as spring length, were limited by the desired performance of comb actuator. On the other hand, backside etching to remove the silicon substrate was also considered to improve the yield of devices. However, the large open region of backside etching will cause the silicon and buried oxide to be broken due to the residual stresses [32] [33]. Therefore, a new approach for backside etching was proposed to increase the yield of fabrication. As illustrated in Fig. 3-6, only a rectangular ring was etched by DRIE in the backside (Fig. 3-6 (a)). After the backside etching, the oxide layer could be

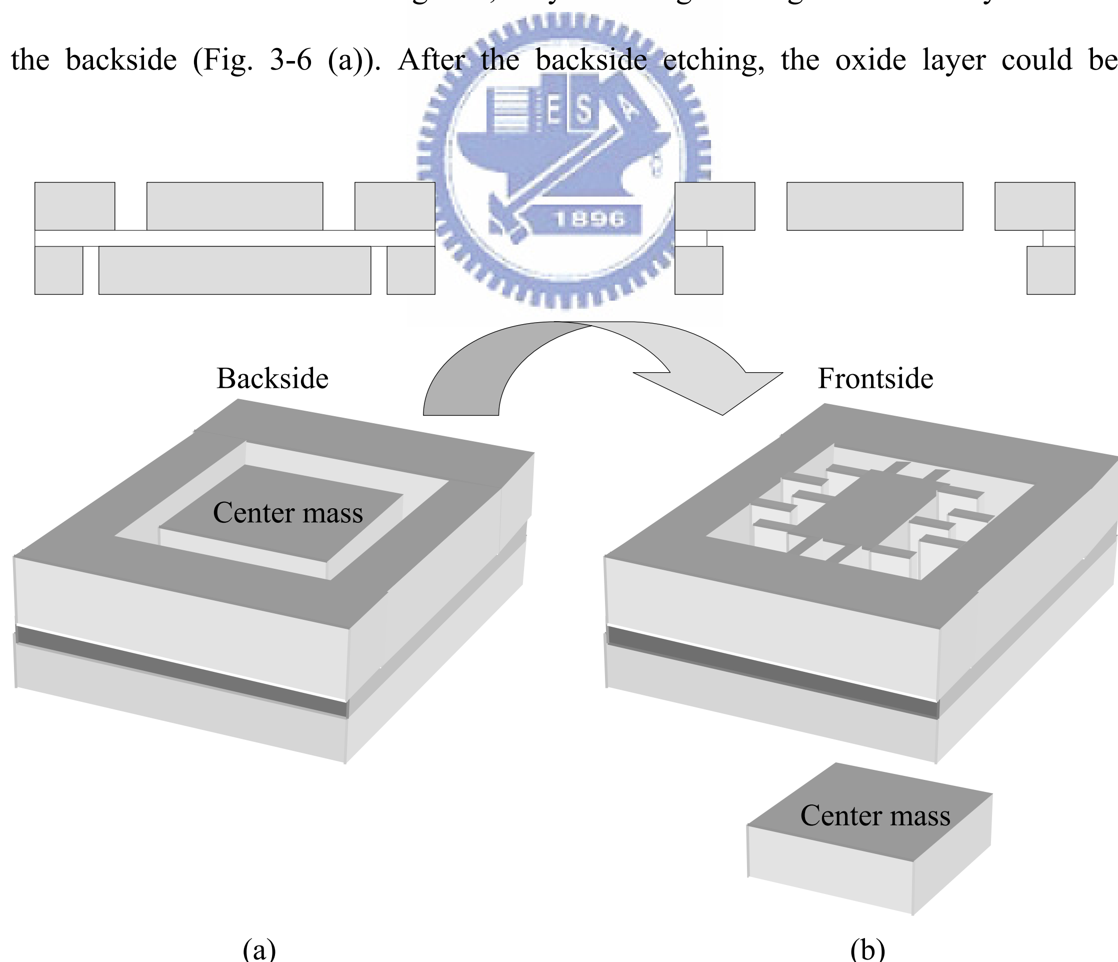

Fig. 3-6 A new approach for backside etching, (a) rectangular ring RIE (backside view) (b) sacrificial layer removal (frontside view)

removed by HF vapour or BOE. The center silicon mass in the backside inside the rectangular ring was dropped during the release etching (Fig. 3-6 (b)) to achieve the same goal.

With this approach, the frontside silicon structures were preserved during and after DRIE and the effect of the residual stress of the buried oxide could be avoided. Problems in the conventional fabrication double side DRIE, such as poor cooling and the leakage of helium caused by backside through-etching, were also solved by using the new approach. Thus, the fabrication process was modified and a new mask was added to remove the backside silicon, as shown in Fig. 3-7, where the first fourth steps was as in the original process. The sequence of implanted ion was exchanged for p-type wafer (original n-type). After removing the photoresist in Fig. 3-7 (d), a thick photoresist was coated on the frontside to protect the pattern when performing backside photolithography (Fig. 3-7 (e)). AZ9260 was used to form a 10 μm thick hard mask for backside silicon DRIE (Fig. 3-7 (f)). The rectangular ring on the backside was defined by the 4th photolithography. Then the 5th photolithography (original 4th photolithography) was patterned to define the device structure on the frontside (Fig. 3-7 (g)). The frontside DRIE was performed before the backside DRIE (Figs. 3-7 (h),(i)). After dicing, the chip sample was released by pure HF vapour (Fig. 3-7 (j)). The detail of process parameters are shown in Table 3-2.

Successful fabrication demonstrated the feasibility of the proposed. Fig. 3-8 (a) and (b) are the frontside and backside views of a comb before release etching. A 50 μm wide rectangular ring can be clearly seen. After 4 min HF vapour, the backside rectangular silicon dropped, as shown in Fig. 3-8 (c) (d). Finally, the sample was baked after IPA rinsing to complete the fabrication process. Thus, the new release approach has a low risk and high yield compared with the conventional way of etching the whole block under

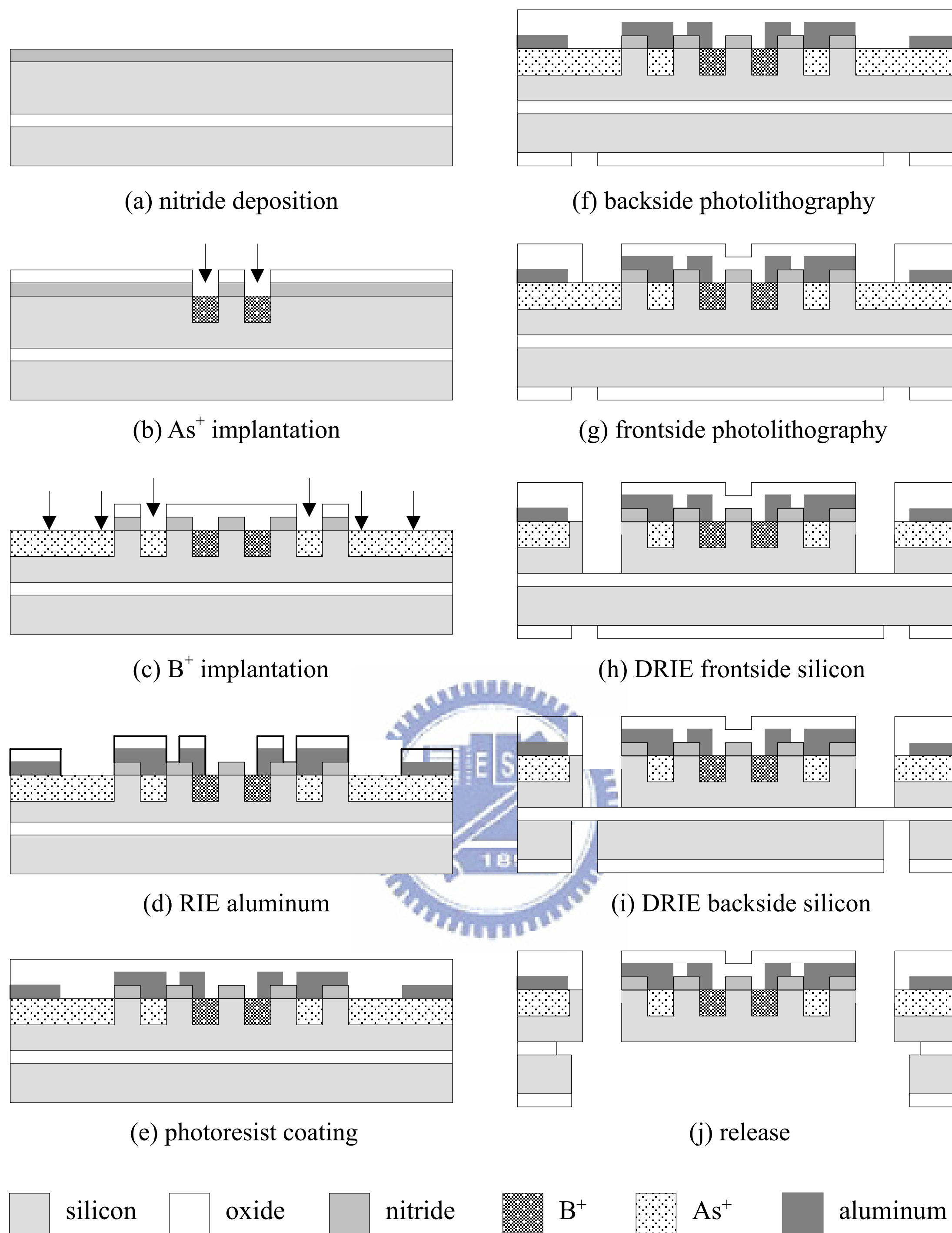

Fig. 3-7 Modified process (a) LPCVD nitride (b) As^+ ion implantation (c) B^+ ion implantation (d) Al patterning (e) protection layer coating (f) backside photolithography (g) frontside photolithography (h) frontside DRIE (i) backside DRIE (j) release

the suspended area.

Table 3-2 Modified SOI process and parameters

step	action	parameter	thickness/depth	place
1	RCA clean			
2	LPCVD Si_3N_4	800°C, 180 mTorr SiH_2Cl_2/NH_3=105:35	3500 Å	SRC
3	1st photolithography	FH6400 exposure 30s with filter	0.8 μm	SRC
4	RIE Si_3N_4	50 mTorr, 100W $SF_6:CHF_3$=30:10	3500 Å	SRC
5	As ion implantation	dose $3\times10^{15}/cm^2$, 30KeV		NDL
6	activate with RTA	900°C, 10s		SRC
7	remove photoresist	O_2 plasma 5 min		SRC
8	2nd photolithography	FH6400 exposure 30s with filter	0.8 μm	SRC
9	RIE Si_3N_4	50 mTorr, 100W $SF_6:CHF_3$=30:10	3500 Å	SRC
10	B ion implantation	dose $3\times10^{15}/cm^2$, 60KeV		NDL
11	activate with RTA	900°C, 15s		SRC
12	remove photoresist	O_2 plasma 5 min		SRC
13	metallization	thermal coat aluminum	5000 Å	SRC
14	3rd photolithography	FH6400 exposure 30s with filter	0.8 μm	SRC
15	RIE Al	10 mTorr, 120W $BCl_3:Cl_2$=40:40	5000 Å	SRC
16	remove photoresist	O_2 plasma 5 min		SRC
17	photoresist coating	AZ4620	6 μm	SRC
18	4th (backside) photolithography	AZ9260 (operated by ITRI)	10 μm	ITRI
19	5th (frontside) photolithography	FH6400 1st spin 500 rpm 2nd spin 1500 rpm soft bake 3 min exposure 45s with filter post bake 20 min	2 μm	SRC
20	DRIE Si (frontside)	operated by CSUN	20 μm	CSUN
21	DRIE Si (backside)	operated by CSUN	400 μm	CSUN
22	dicing			

23	release	HF vapour 4 min	2 μm	SRC
24	IPA cleaning	5 min rinse		SRC
25	remove photoresist	O_2 plasma 10 min		SRC

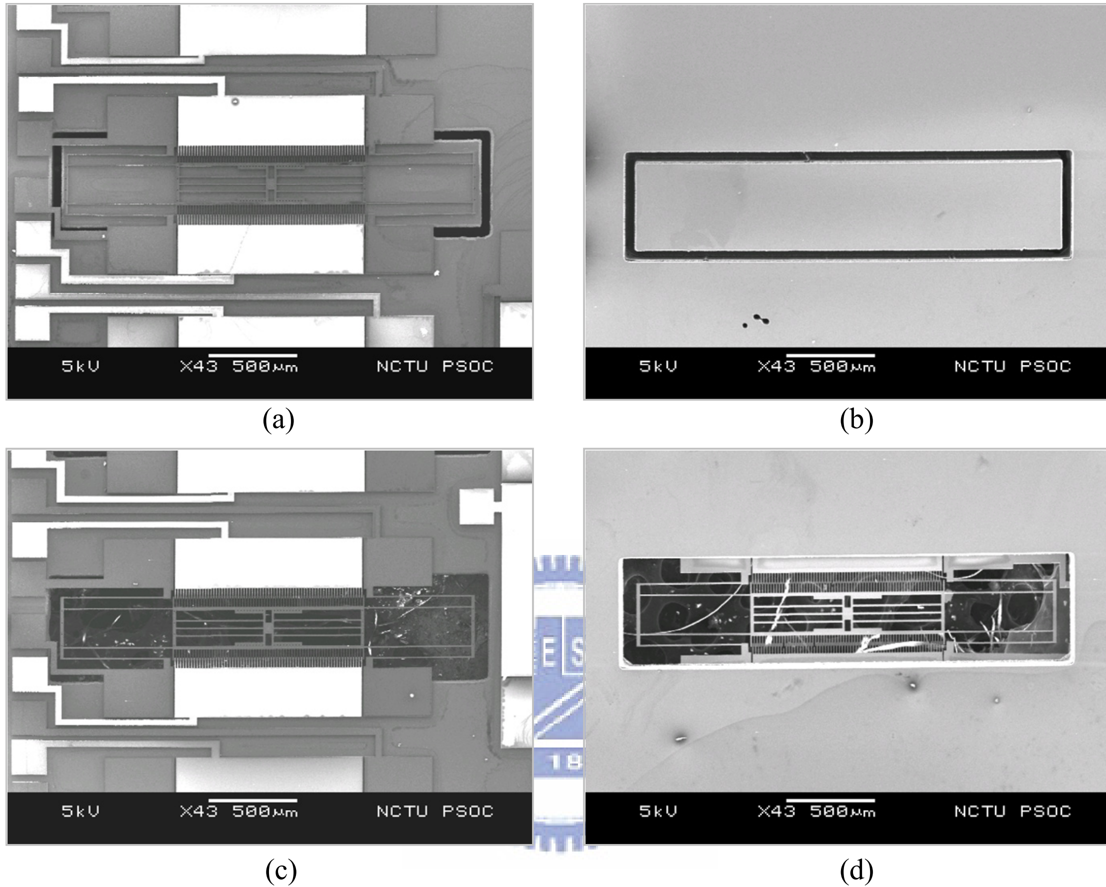

Fig. 3-8 (a) Frontside view and (b) backside view before release; (c) frontside view and (d) backside view after release

3.2.4 Fabricated SOI devices

A comb actuator with a photo detector for the absorption type and reflection type device was fabricated in the SOI process. Using the proposed release approach, the backside etching was achieved after the center mass is dropped. The suspended structures (Fig. 3-9 (a)) were fabricated with high yield. A top view of the whole device was shown in Fig. 3-9 (b). With the decreased release time, the aluminum was mostly preserved in the modified process. The metal line of 4 μm width was patterned on the springs of 10 μm as we expected. Two type of knife edge detectors were

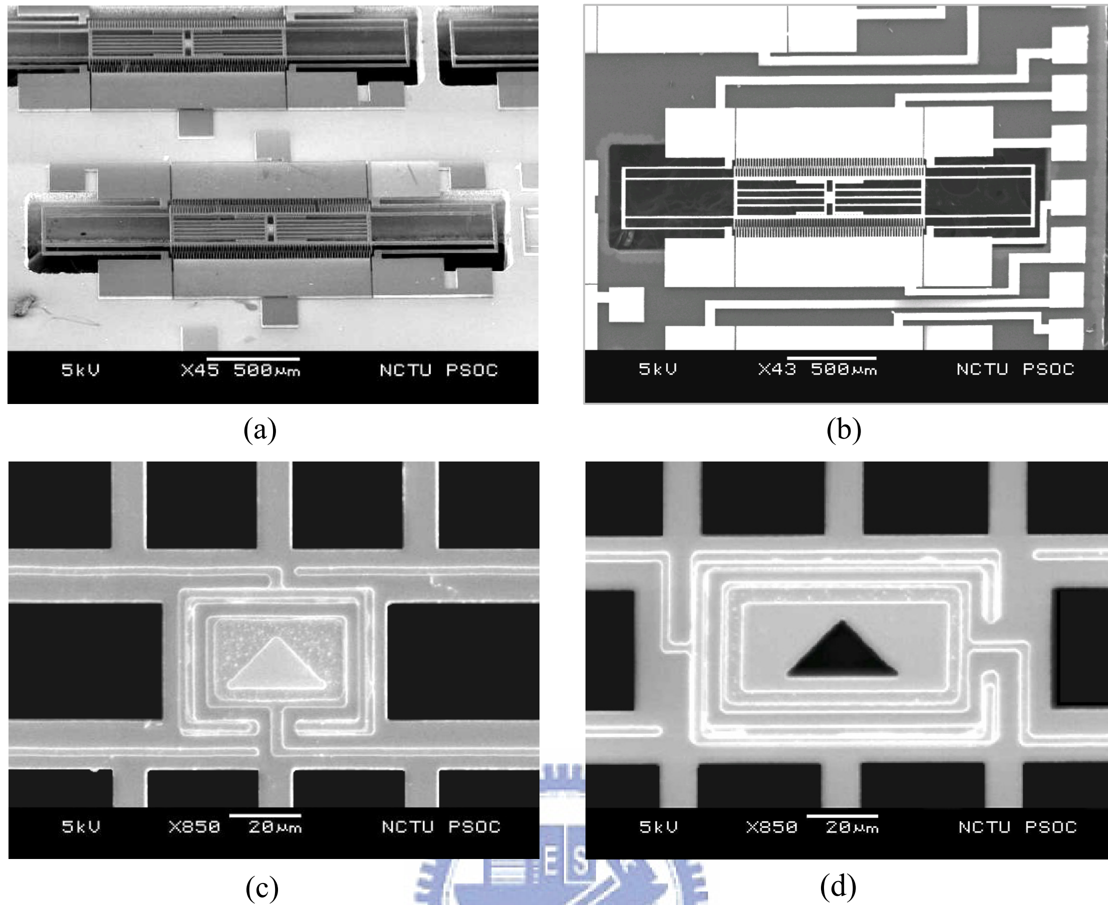

Fig. 3-9 SEM of fabricated devices: (a) Fabricated devices (b) top view of a comb (c) type-1 knife edge detector (d) type-2 knife edge detector

fabricated. In type-1, the optical distribution can be sensed by the triangular silicon region while the part of the light distribution is blocked and reflected by the aluminum film (Fig. 3-9 (c)). Another design was shown in Fig. 3-9 (d). The triangular etched-through region is used as the knife edge plate for reflection type. Light can be reflected by silicon plate for the reflection type device, or absorbed by the ion implanted photo detector for the absorption type device.

3.3 Post CMOS process

For the absorption type device, the photo detectors, comb actuators, and amplifying circuits are fabricated in the CMOS process. However, extra post

fabrication steps are needed to release the suspended structure. A cross section view of the components in CMOS MEMS process is shown in Fig. 3-10 and a post process flow is proposed in Fig. 3-11. It is a maskless process using only dry etching. The photo detector is preserved using different patterns in the metal hard mask layers.

The CMOS process is supported by CIC using the TSMC 2P4M 0.35 μm process (Fig. 3-10). The circuits for signal processing are far away from the suspended comb actuator. After the completion of the standard CMOS process, the 2×2 mm^2 chip is bonded to a 4″ wafer by a vacuum tape for post fabrication. The first step is backside etching. As shown in Fig 3-11 (a), the substrate is etched until a 5-μm-thick layer of silicon is left to ensure the normal operation of the photodiode. The second step is the anisotropic etching of the frontside dielectric layer (Fig. 3-11 (b)). The comb structure is defined by patterns in the metal-4 layer. The metal layer is removed in the third step. As shown in Fig. 3-11 (c), the exposed oxide is used as the hard mask for the following isotropic etching of silicon in the fourth step. By the high selectivity of SF_6 between oxide and silicon, the silicon substrate is undercut and suspended (Fig. 3-11 (d)). The isolation of electrical signals is also achieved when the silicon under

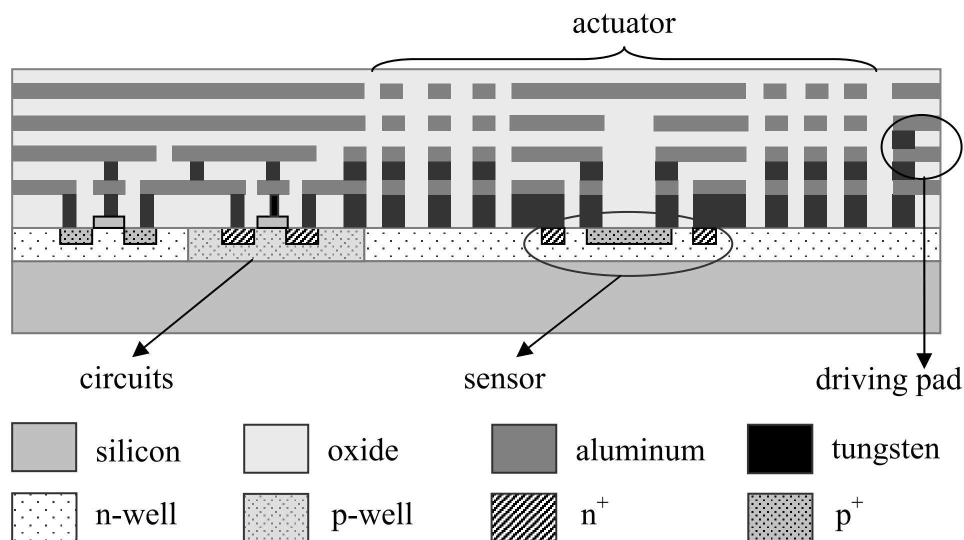

Fig. 3-10 Cross section view of CMOS process and components of device

the suspended structure is removed at the same time. The photodiode is protected by the oxide layer in this step. The fifth step is the anisotropic etching of the oxide layer until metel-3 is exposed. At this step, the detection region of the photodiode and

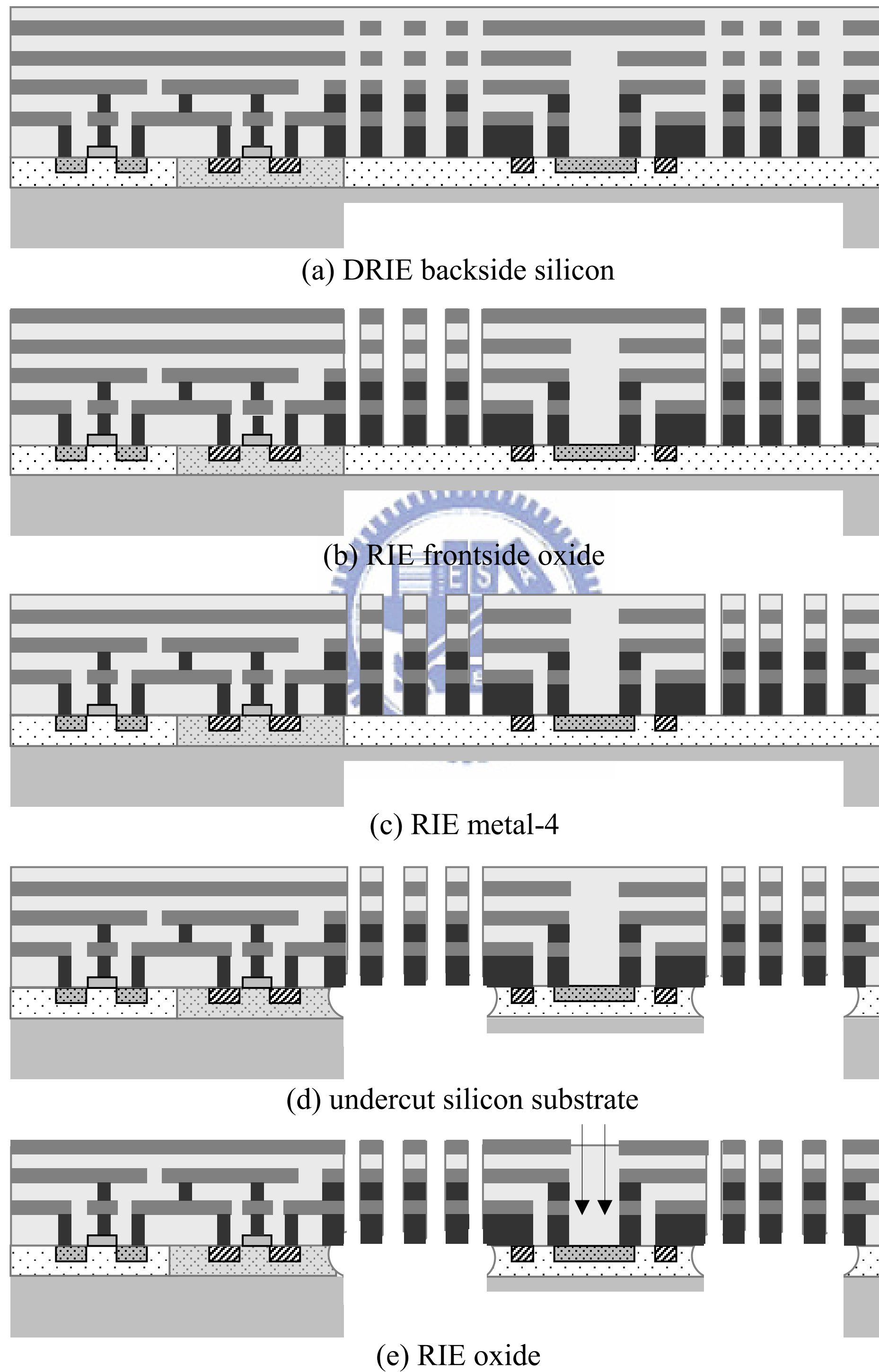
(a) DRIE backside silicon

(b) RIE frontside oxide

(c) RIE metal-4

(d) undercut silicon substrate

(e) RIE oxide

Fig. 3-11 Post CMOS fabrication process (a) backside etch (b) anisotropic dielectric etch (c) metal etch (d) isotropic silicon etch (e) anisotropic dielectric etch

the pad for electrical conduction is opened (Fig. 3-11 (e)). Finally, the post process is completed and the chip is taken from the wafer for further testing.

3.4 Post process testing

For the feasibility of the post process, a similar but simpler testing process was used to simulate the issues to be encountered in actual fabrication. Three issues were integrated. In the first experiment, photolithography for backside etching of a died chip was tested and verified. Then an isotropic etch of silicon was performed to find out the suitable process parameters for a better undercut profile. At last, oxide of 5 μm and aluminum of 5000 Å were deposited to simulate the proposed dry etching post process. The micromasking effect caused by the metal mask was reduced, as will be shown in Section 3.4.3.

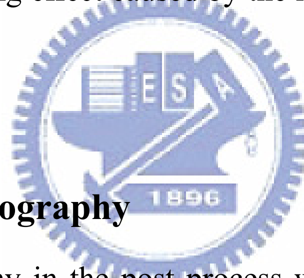

3.4.1 Backside photolithography

The only photolithography in the post process was for the backside etching of silicon under the suspended structures. A 1100×1600 μm^2 CMOS chip was used in the experiment, whereas the actual chip area from CIC is 1600×2200 μm^2. In the beginning, the chip was bonded to a 4″ wafer by the vacuum tape. A thin film photoresist, FH6400, was used to find out the limitation of the line width in backside photolithography of a die. The bonded chip was surrounded by other chips to ensure the uniform and flat photoresist coating. As an important factor, photoresist of precisely-controlled thickness is the key point in die photolithography. After soft bake and exposure, the chip was developed in FHD5 for only a few second. The result of photolithography was observed by an optical microscope and is shown in Fig. 3-12. Clear patterns can be seen. A 6000 Å dry etching was performed to examine the

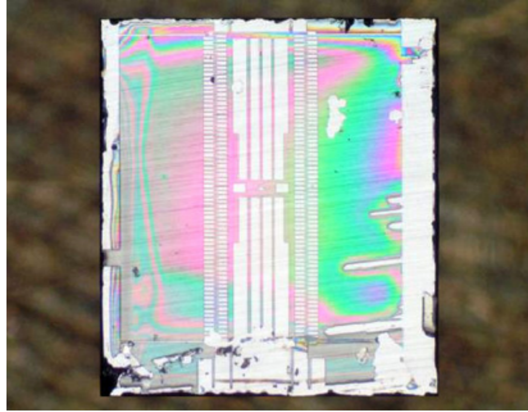

Fig. 3-12 Pattern on a CMOS chip of size 1.1×1.6 mm^2

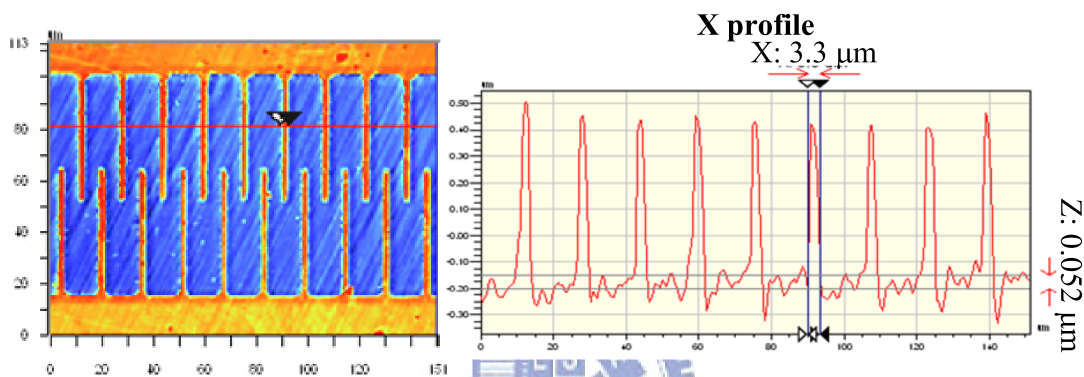

Fig. 3-13 Etching profile by WYKO

feasibility of backside DRIE. The photoresist was then removed by O_2 plasma after RIE. The test sample observed by a WYKO interferometer showed a well etched profile, as shown in Fig. 3-13. The unevenness of the surface was due to the unpolished backside of the wafer. The finger width was reduced from 4 μm to 3.3 μm. The error was acceptable as the tolerance of width loss was 20 μm in a actual pattern of a rectangular area of 200×200 μm^2.

3.4.2 Isotropic silicon etching

In the post process, isotropic silicon etching is performed after the anisotropic dielectric etching to isolate the electrical signal and release the structure. The silicon under the oxide layer will result in a short circuit. For the absorption type device, the isolation is especially important to avoid the interference of signals between the

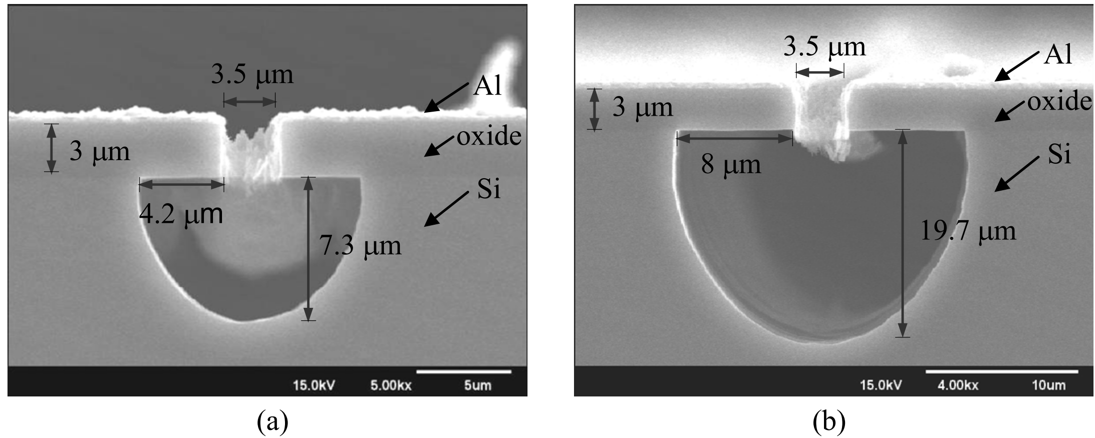

(a) (b)

Fig. 3-14 SEM of undercut profile for (a) 10 minutes (b) 20 minutes

actuator and the sensor. In the layout design of CMOS device, the width of the suspended mesh beam is 4 μm. In [33], the undercut profile using SF_6 showed a good result with no residual silicon under the oxide after etching. Thus, experiments were conducted to undercut a beam of 4 μm (the actual width in our design) by using pure SF_6.

The experiment began with a sample with 3 μm PECVD oxide on top. A 5000 Å aluminum with a 3.5 μm opening was used as the hard mask. The SEM of a laterally etched profile is shown in Fig. 3-13. With a chamber pressure of 50 mTorr and pure SF_6 flow of 50 sccm, undercut range of 4.2 μm and 8 μm were obtained for the process time of 10 minutes (Fig. 3-14 (a)) and 20 minutes (Fig. 3-14 (b)), respectively. The range of isotropic etch was large enough to release the structures.

3.4.3 Anisotropic oxide etching

A test process for etching the dielectric and metal layers of CMOS was performed. As shown in Fig. 3-15 (a), a 5000 Å aluminum was coated are patterned on a 5 μm thick PECVD oxide, which has the same thickness as the 4 aluminum and 4 oxide layers in the CMOS process of (Fig. 3-15 (b)). After the process to etch the oxide of 5 μm, the SEM result is shown in Fig. 3-16 (a). Serious micromasking effect

was observed and the anisotropic etching could not go on because of the large mount of RIE grass on the substrate surface [34].

To solve the problem, the chip was rinsed in IPA to clean the surface after every 2 μm oxide etching. Some polymer was removed during the rinse and a smooth substrate was obtained (Fig. 3-16 (b)). Still RIE grass remained on the surface, but the oxide was mostly removed and the next isotropic silicon etch could be performed. After 10 minutes of isotropic etching, the substrate silicon was removed. Detailed fabrication parameters are listed in Table 3-3. The SEM results of the successfully released anchor and fingers are shown in Fig. 3-17. From above, the process parameters were found and the feasibility of the post fabrication was demonstrated.

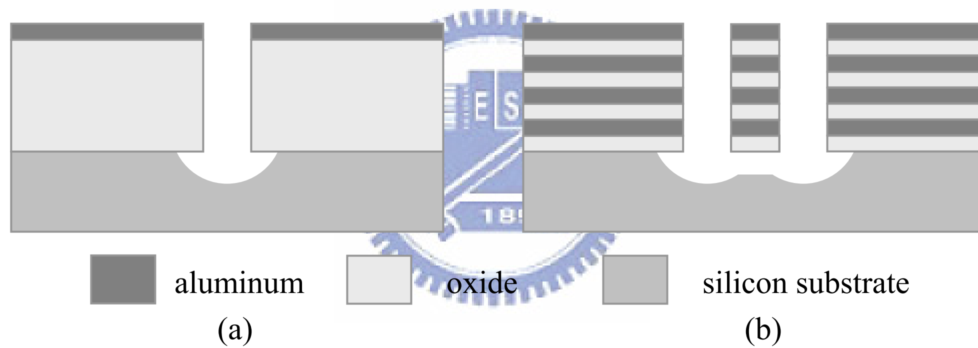

Fig. 3-15 Cross section view of: (a) testing process (b) CMOS process

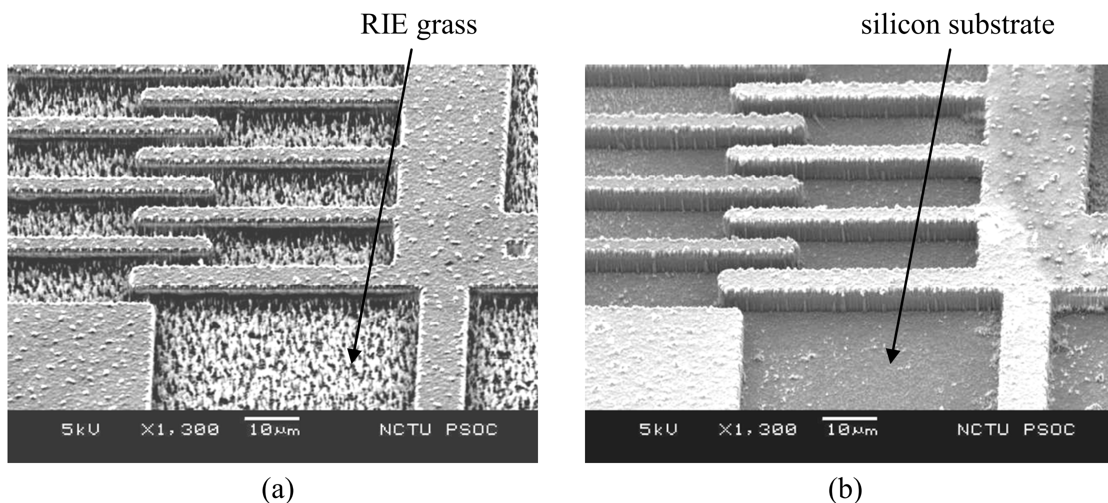

Fig. 3-16 SEM of the RIE grass (a) without IPA rinse (b) with IPA rinse

Table 3-3 Detailed fabrication parameters of test experiments

step	action	parameter	depth	comment
1	RIE oxide	CHF_3 flow 40 sccm Ar flow 40 sccm 10 mtorr, 750W, 30 min	5 μm	Divided into 3 times IPA rinse in each step
2	RIE silicon (isotropic)	SF_6 flow 50 sccm 50 mtorr, 120W, 10 min	undercut depth: 4.2 μm vertical depth: 7.3 μm	

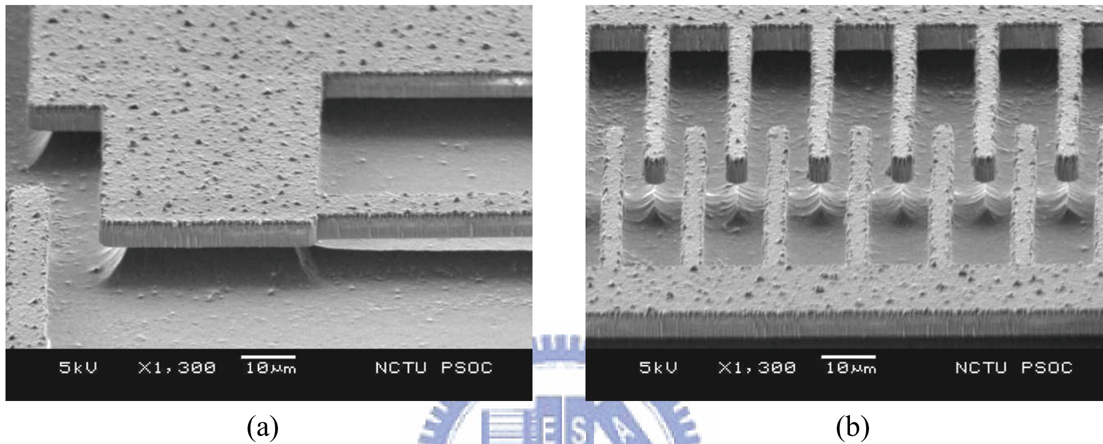

(a) (b)

Fig. 3-17 SEM of released structure (a) anchor (b) fingers (gap spacing = finger width = 4 μm)

3.5 Summary

In this chapter, the SOI and post CMOS processes for the absorption type device are presented. A new approach for the backside dry etching was proposed and demonstrated with fine results. The SOI device was successfully fabricated. The test experiments for post CMOS process were performed to find out the desired parameters. The results showed the capability and feasibility to handle the post fabrication.

Chapter 4 Experiment Results and Measurement

The two main components of the micro optical profile measurement system, the comb actuator and the photo detector, were measured and analyzed. The measured data of the SOI device is presented.

4.1 Comb drive actuator

The characteristics of the fabricated comb drive actuator was observed. Using an optical microscope and measured by a MEMS motion analyzer (MMA). The oscillating electrostatic force was generated by placing a DC (V_{DC}) and an AC (V_{AC}) voltage sources in serious across the fixed and the movable electrodes of the comb actuator. Under V_{DC} of 15 V and V_{AC} amplitude of 15V, the resonant frequency of the lateral mode was found at 7.133 kHz. The vibration of the scanning knife edge photo detector is shown in Fig. 4-1. The amplitude and phase of the frequency response under driving voltage was measured and plotted in the Fig. 4-2, the maximum amplitude of 10 μm was found at 7.133 kHz and a phase shift of 180° was also observed across resonance frequency. From the measured data, the 3dB bandwidth

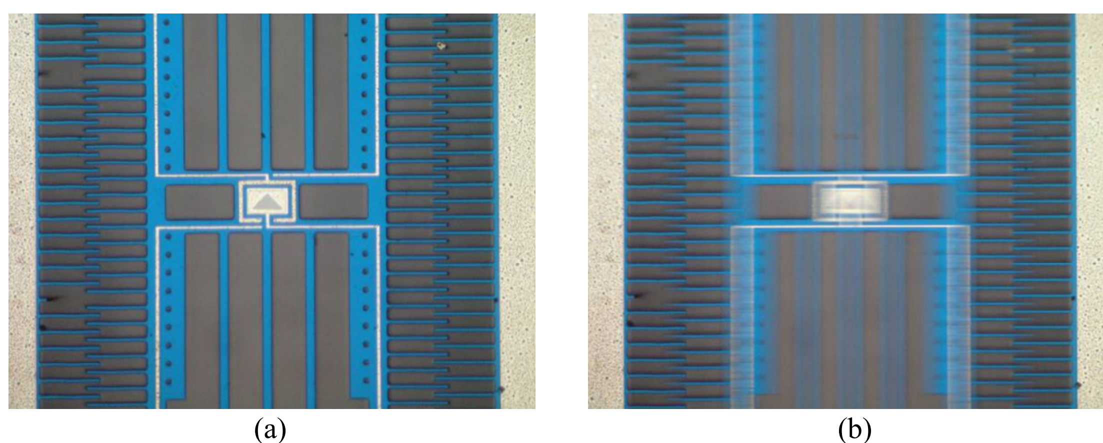

(a) (b)

Fig. 4-1 Images of (a) fabricated device (b) operation at resonance

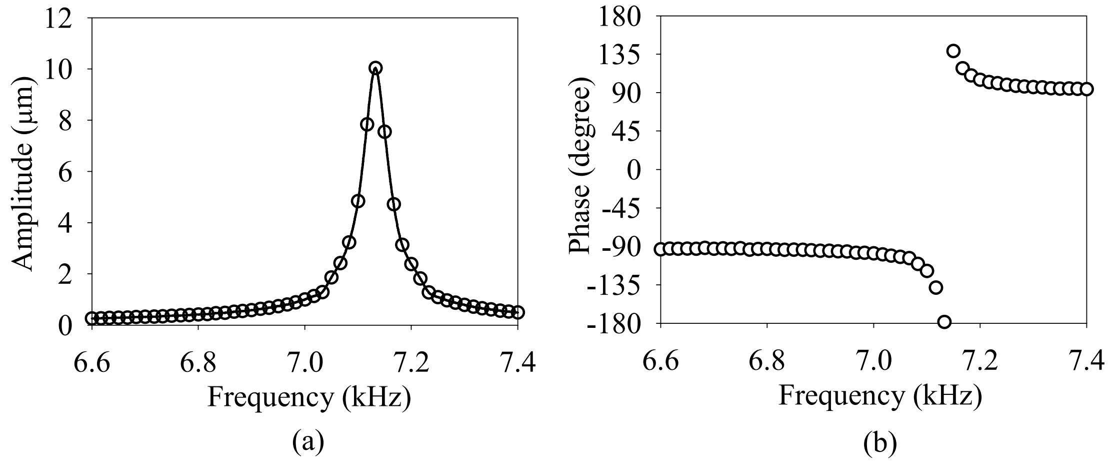

(a) (b)

Fig. 4-2 Frequency response of (a) amplitude (b) phase

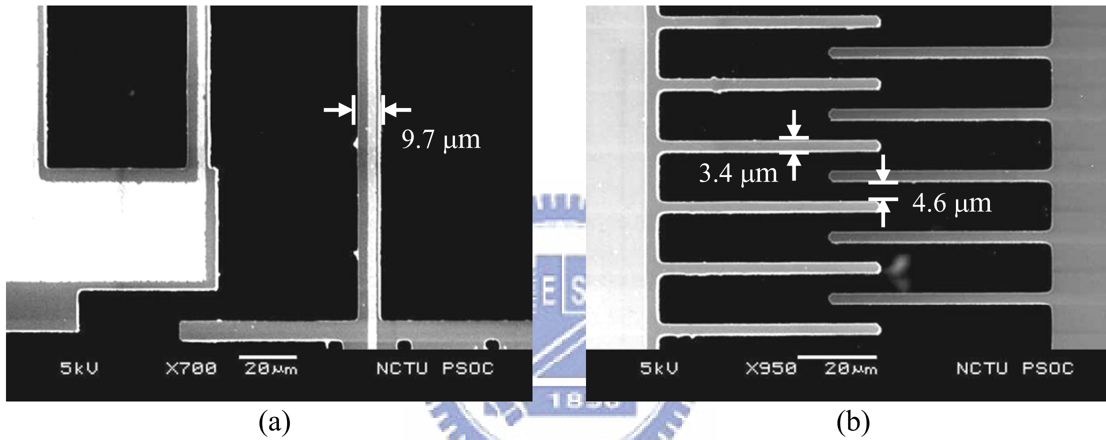

(a) (b)

Fig. 4-3 The width of (a) spring (b) finger

was 0.052 kHz and thus the quality factor Q was found to be 137. The measured resonant frequency of 7.133 kHz was a little less than the simulation value of 7.58 kHz. The main reason was the loss of spring width from 10 μm to 9.7 μm (Fig. 4-3 (a)) caused by the error of photolithography.

The displacement of the actuator can be expressed as $2\frac{n\varepsilon_0 h}{gk_x}V_{DC}V_{AC}Q$, as discussed in Section 2-5. In our experiment, the DC voltage V_{DC} is equal to the amplitude of AC voltage V_{AC}, $V_{DC} = V_{AC}$. The actual displacement at resonance measured by the MMA is plotted with the theoretical value in Fig. 4-4. The measured results are less than the theoretical values caused by the loss of finger width. Thus, the

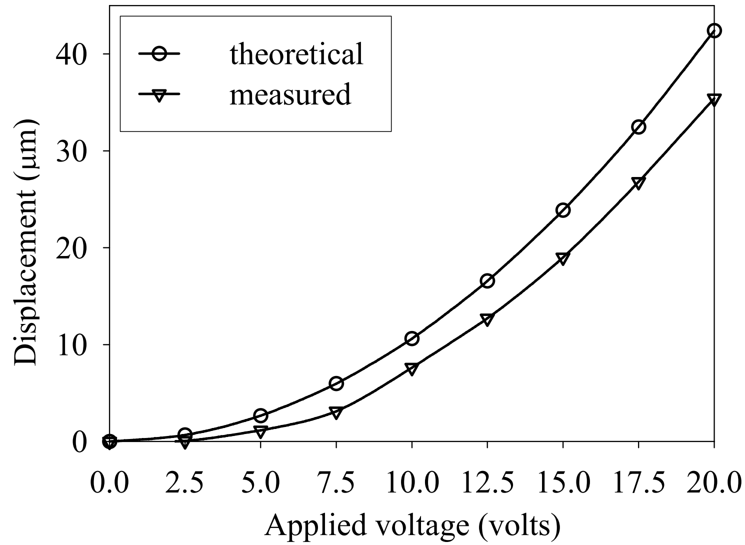

Fig. 4-4 Displacement under the applied voltage ($V_{DC}+V_{AC}$)

larger gap spacing of 4.6 μm (Fig. 4-3 (b)) was measured instead of the original spacing of 4 μm. From the figure, a displacement of 20 μm for knife edge can be obtained at V_{DC} =15 V and V_{AC} =15 V.

4.2 Characteristics of photo detector

The characteristics of the photo detector were measured by a Keithley 4200 semiconductor analyzer system. The fabricated results of a testing photo detector are shown in Fig. 4-5. The triangular n^+ region was 600 μm in bottom and 300 μm in height. The I-V curves of the photo detectors in three runs were recorded and are discussed below.

The optical power in the 1.33 cm^2 illuminated area under the microscope is 7.2 mW with the power meter set for 600 nm wavelength. The results of the photo detectors in the first and the second runs are plotted in Fig. 4-6. The improvement of photocurrent in the second-run photodiode compared with the first run devices is mainly due to the using of lower substrate concentration N_S (from 10^{17} cm^{-3} to 10^{15} cm^{-3}). Under the condition, a wider depletion was obtained and thus the photocurrent

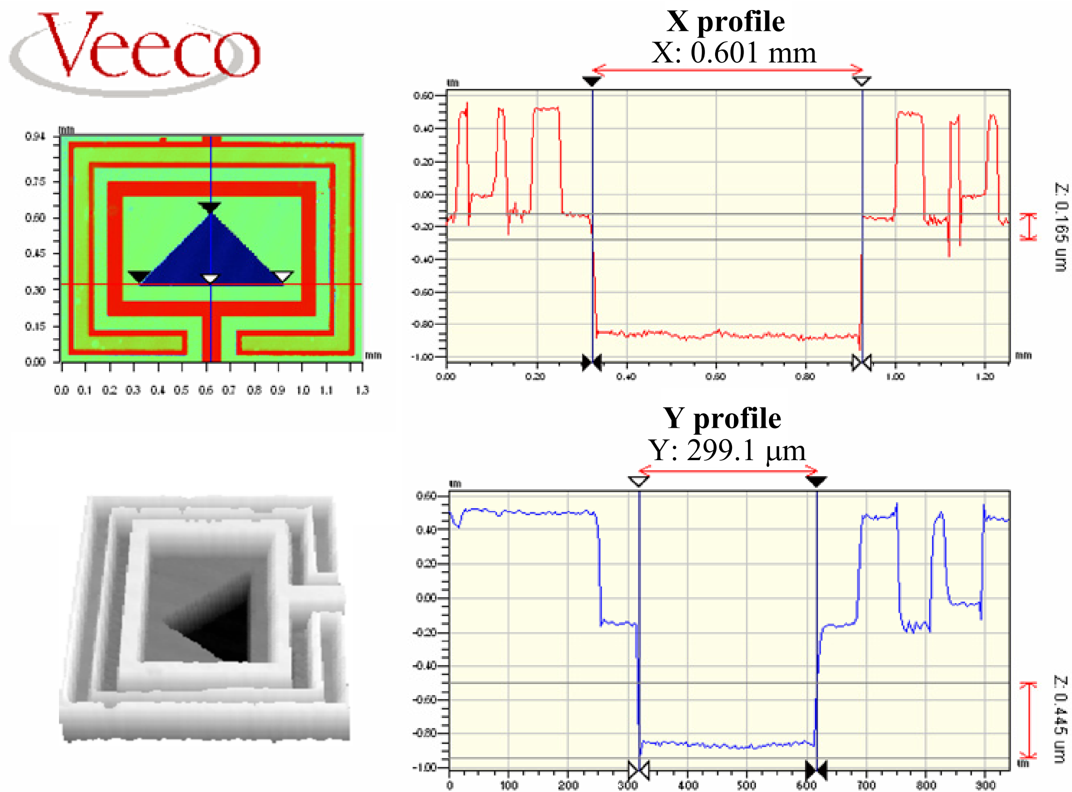

Fig. 4-5 Area of testing diode measured by a WYKO interferometer

was increased. The photocurrent of second run detector was thus larger than the first run detector by a factor of 45 (Fig. 4-6 (a)). The transition from reverse blocking state to breakdown region can be observed in the first run diode under bias voltage of 10 volts. The low breakdown voltage is caused by the high doping concentration of the substrate N_S since the breakdown voltage is inversely proportional to N_S. An approximately value of breakdown voltage under $N_S = 10^{17}$ cm^{-3} is 15 volts [29]. For precise calculation, the doping concentration of p^+ (to form p^+-n junction) will also decrease the breakdown voltage.

The effects processing steps of the photo detectors were also investigated. Whether the high process temperature influences the diode performance in the process is an interesting issue. The I-V curve of third run photo detector was recorded after metallization (Fig. 4-7 (a)). As described previously, frontside DRIE and backside

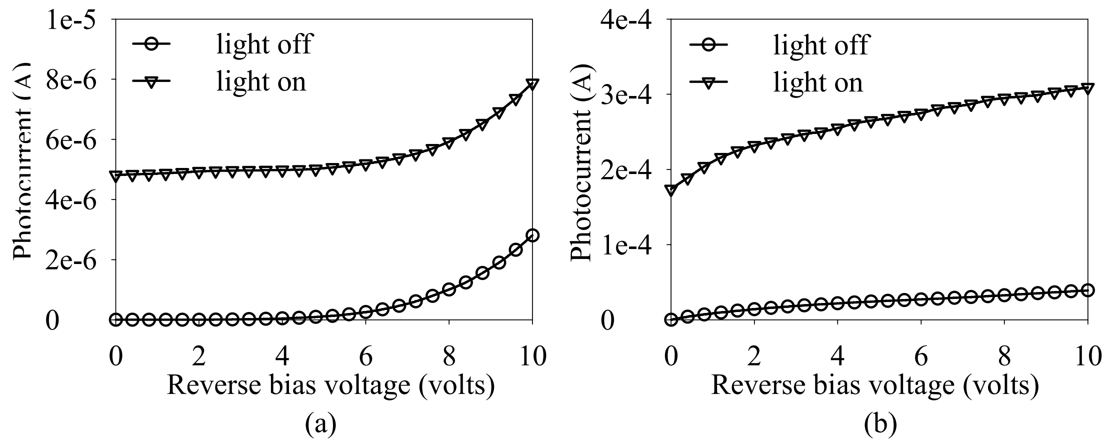

Fig. 4-6 Measured photocurrent of: (a) first run photo detector ($N_S = 10^{17}$ cm^{-3}) (b) second run photo detector ($N_S = 10^{15}$ cm^{-3})

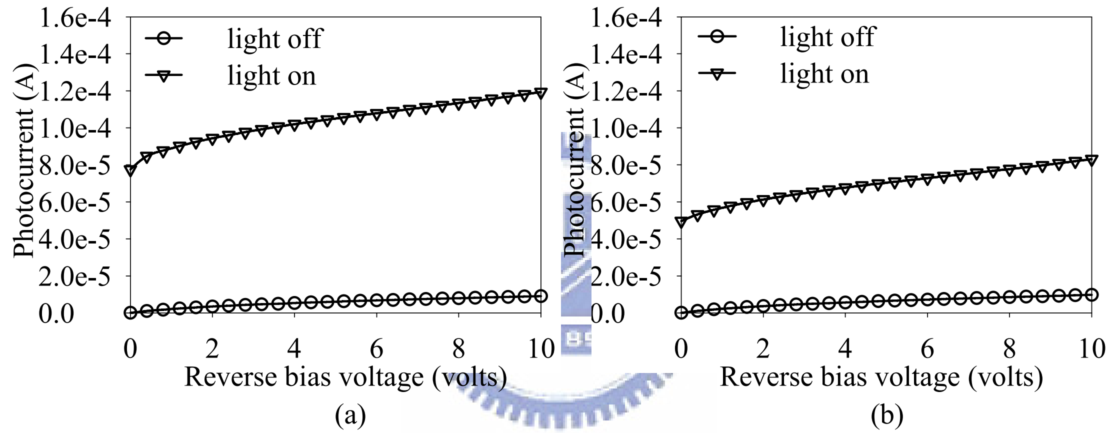

Fig. 4-7 Measured photocurrent of third run photo detector after: (a) metallization (b) ICP and release steps

DRIE were then performed after metallization. It is known that the silicon etching by F^+ ions is an exothermic reaction. The temperature can be achieved to a hundreds of degree various with the material layers above the wafer and the process recipe. The characteristics of the third run photo detector after double side DRIE, release, and photoresist removing are showed in Fig. 4-7 (b). Compared with Fig. 4-7 (a), the results show less photocurrent generated after the following steps. It may be due to the high temperature and long time (about 30 min) DRIE process. The leakage current caused by unclean surface is also the concern. Even then, the properties of a photo

detector are mostly preserved after the proposed SOI fabrication process.

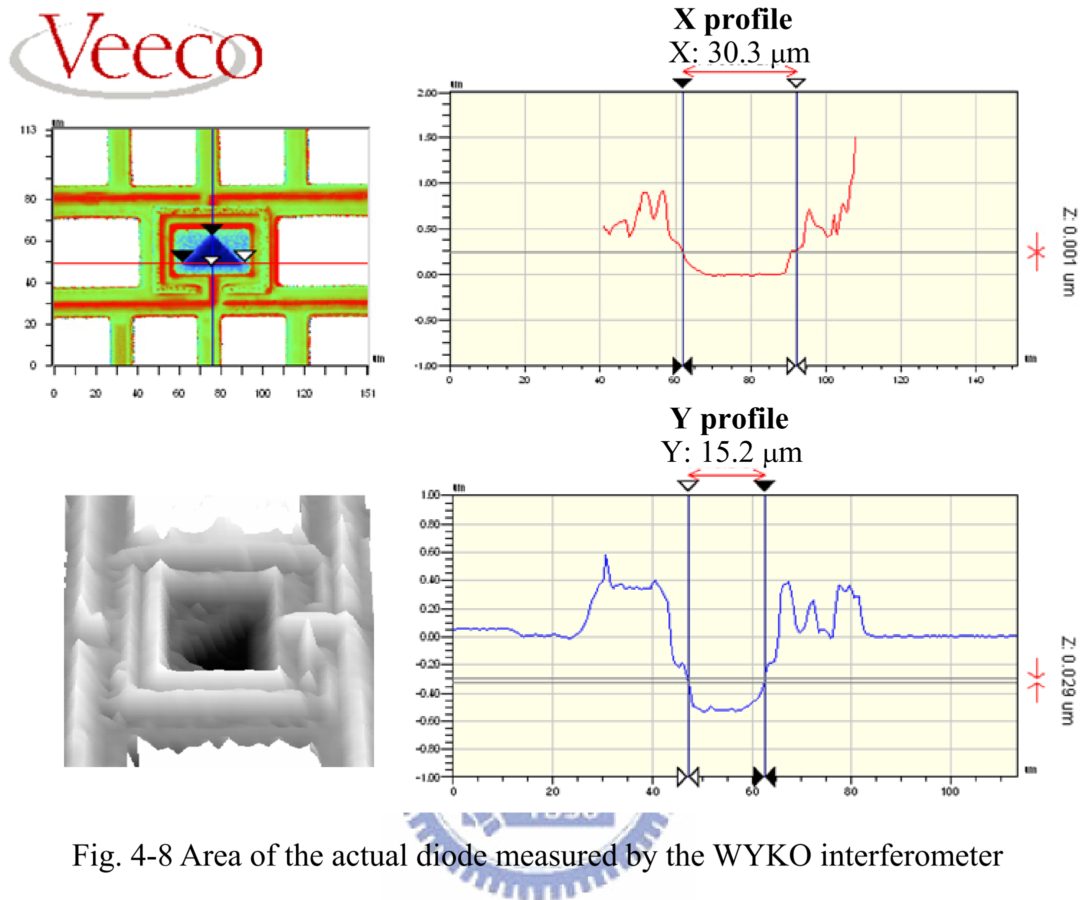

Fig. 4-8 Area of the actual diode measured by the WYKO interferometer

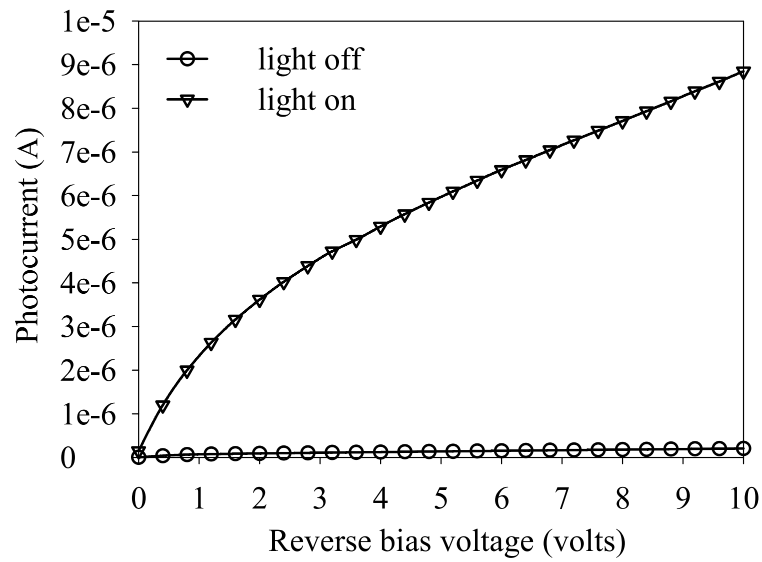

Fig. 4-9 The I-V curve of the photo detector for absorption type

At last, the actual diodes in the absorption type device were measured. The triangular region of a diode fabricated on comb had a bottom of 30 μm and a height of 15 μm (Fig. 4-8). A rough surface profile was observed due to the bombardment of high energy O_2 plasma. The I-V curve of the photo detector is plotted in Fig. 4-9. The optical intensity is 2.46×10^{-5} mW in the 450 μm^2 detection area. Under a bias voltage of 5 volts, the responsivity can be fond to be 262 A/W.

4.3 Optical profile measurement

For micro optical spot measurement, the He-Ne laser is used as the light source. The micro laser spot focused by an objective lens can be measured by the fabricated device. From the viewpoint of geometric optics, light can be focused into an infinitesimal point if no aberration is presented. However, diffraction limits the minimum spot size due to wave nature of light. The diffraction limit of a focused spots was aimed and can be calculated from [35]:

$$s \cong \frac{0.5\lambda}{NA} \tag{22}$$

where λ is the incident laser wavelength and NA is the numerical aperture. The results measured by fabricated device, including the reflection and absorption types, using

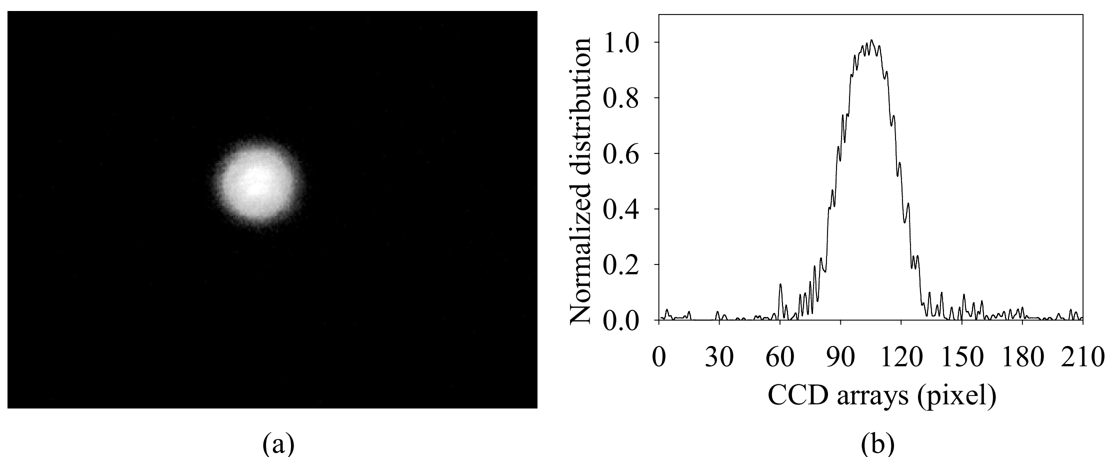

(a) (b)

Fig. 4-10 Focused laser spot: (a) image observed by CCD (b) normalized distribution

different light sources and objective lenses are presented in this section. Before measurement, an optical spot from red He-Ne laser was measured, as shown in Fig. 4-10 (a). The intensity of the spot is close to a Gaussian distribution. However, aberration is found at the left-side of distribution (Fig. 4-10 (b)).

4.3.1 Reflection-type system

The setup for the reflection type spot profile measurement is shown in fig. 4-11. A DC coupled amplified photo detector THORLABS PDA 155 was used to detect the signal from the reflective knife-edge plate. In the optical path, a beam expander expanded the laser beam before entering the focusing objective lens. Thus, the FWHM of the laser beam after the beam splitter can be large enough to fill the aperture of typical 20X and 40X objectives. The laser light sources are 12mW red light (633nm) and 0.8mW green light (543 nm) He-Ne laser.

As mentioned in Section 3.2.4, a flat mirror made in the silicon device layer of the SOI wafer as the knife edge plate. Part of light (Fig. 3-9 (d) and Fig. 4-11) is

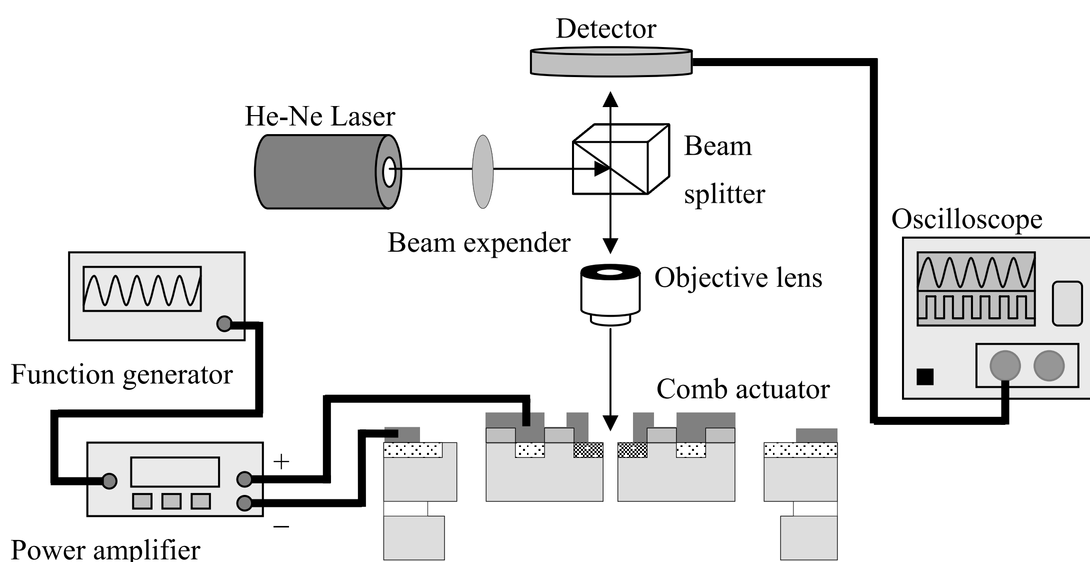

Fig. 4-11 Setup of the reflective type spot profile measurement system

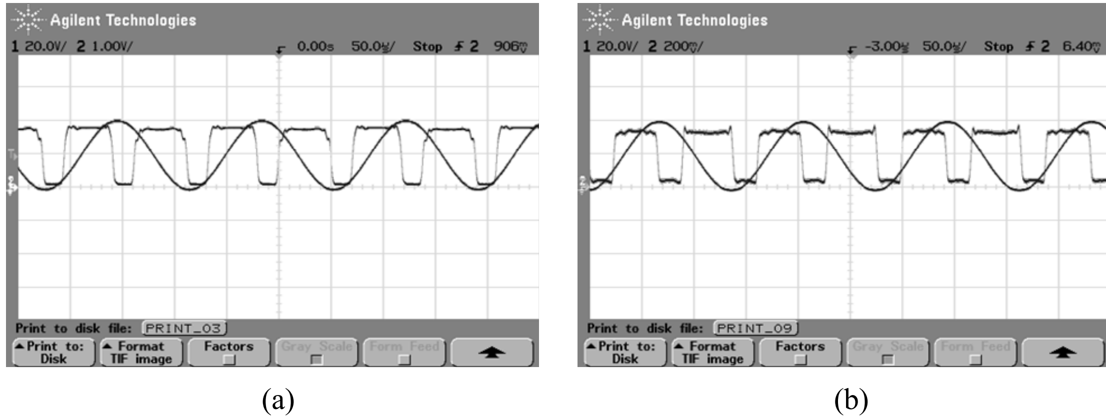

(a) (b)

Fig. 4-12 Observed signals of spots focused with a (a) 20X and (b) 40X objective lens for a 12mW red (633 nm) light laser

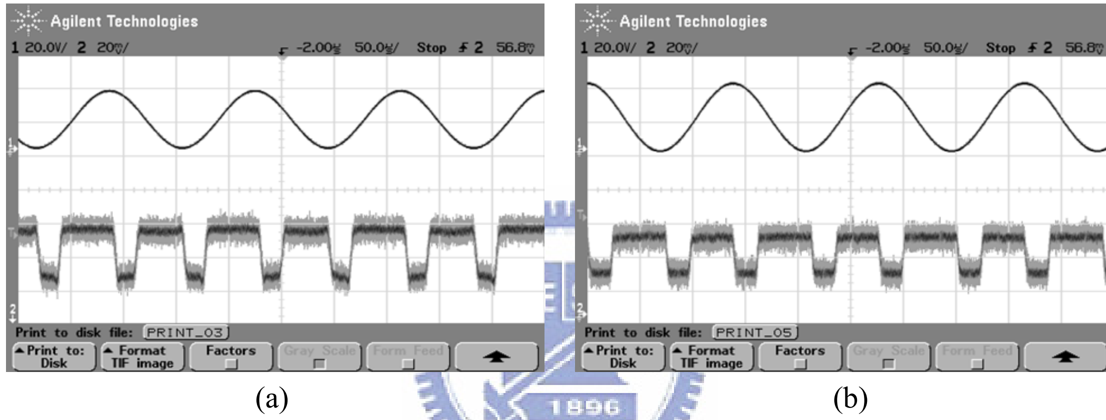

(a) (b)

Fig. 4-13 Observed signals of spots focused with a (a) 20X and (b) 40X objective lens for a 0.8mW green (543 nm) light laser

transmitted through the triangular etched-through region while the other is reflected by the silicon plate. Under the proper driving voltage, the knife edge vibrates periodically. If the vibration amplitude is larger than twice the diameter of focused optical spot, the spot can be scanned in two orthogonal directions in half of the scan cycles. Therefore, four scans of the focused spot distribution can be recorded in one full scan cycle.

To verify the system performance, focused spots made by different light sources and numerical apertures were measured. At resonance, the observed waveforms are shown in Fig. 4-12 and Fig. 4-13. Both the driving voltage and measured photocurrent

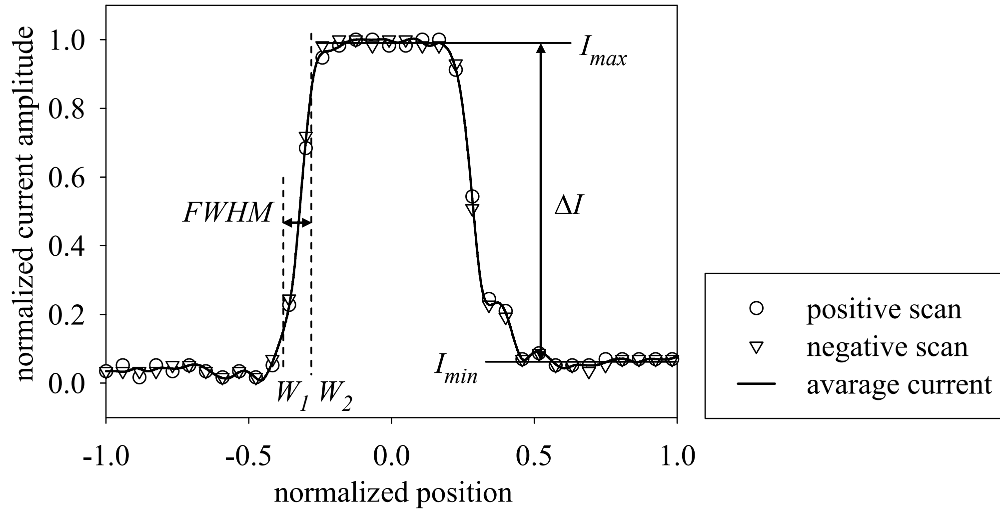

(a) Measured photocurrent amplitude

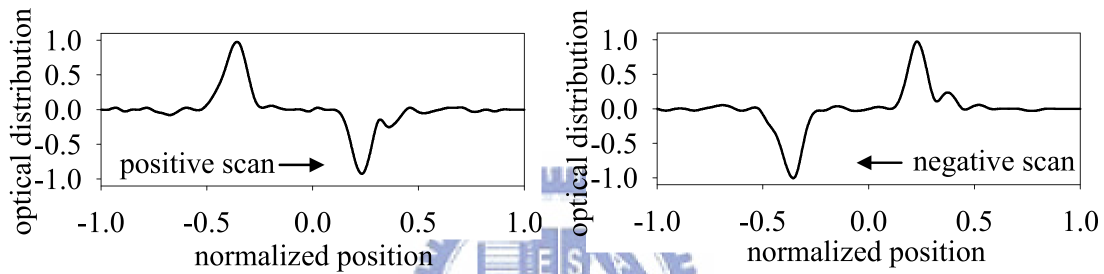

(b) Power distribution in two orthogonal scans

Fig. 4-14 (a) Measured photocurrent and (b) derived power distribution of the spot with 20X objective lens for the red light

amplitude can be observed. Compared to the measurement results in Fig. 4-12, the waveforms in Fig. 4-13 have more noise. The measured current amplitude was in a 10 mV scale. Therefore, electrical interference in transition path was obvious as a lower optical power (0.8 mW) was used. The other irregular peaks in photocurrent waveform are due to the laser noise, interference of the optical path, roughness of the reflective mirror, and the electric noise of photodetector.

From the measured waveforms, the photocurrent of the positive scan and negative scan can be found in one period of the driving sinusoidal wave. For focused spot size calculations, the average photocurrent was acquired and plotted as the first step. A noise reduction filter was used only for the measurement data in Fig. 4-13. All

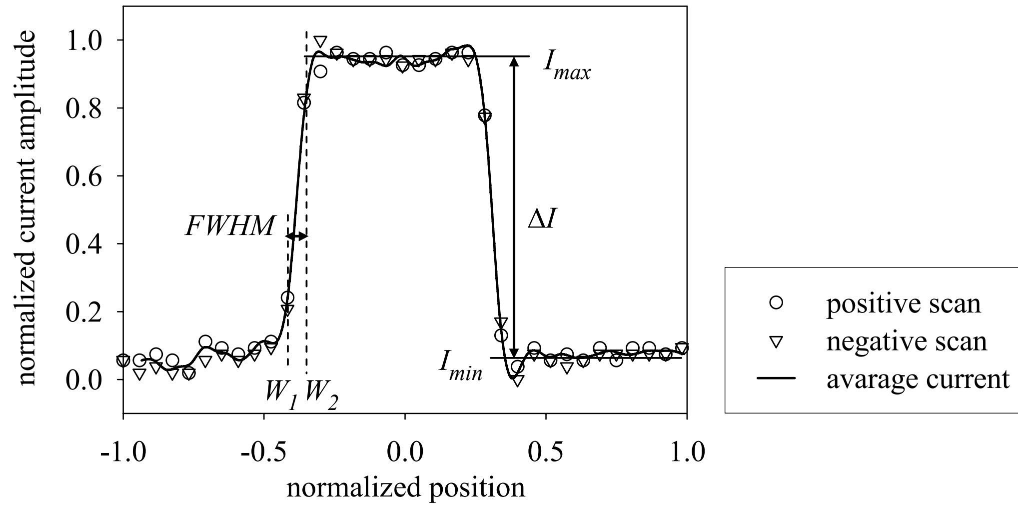

(a) Measured photocurrent amplitude

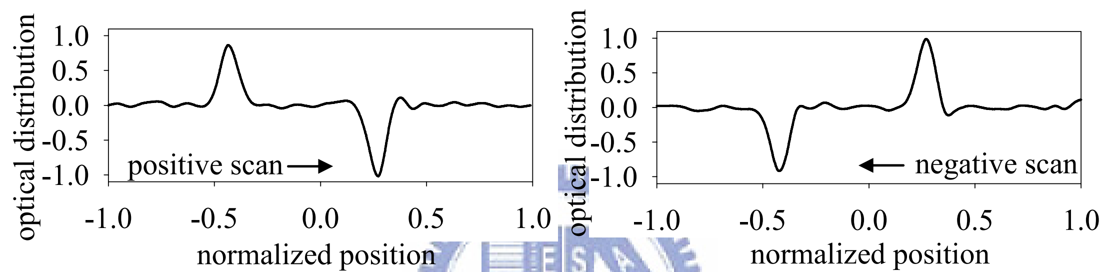

(b) Power distribution in two orthogonal scans

Fig. 4-15 (a) Measured photocurrent and (b) derived power distribution of the spot with 40X objective lens for the red light

the data were measured under a scanning range of ±10 μm, obtained by $V_{DC} = 15V$ and $V_{AC} = 15V$.

Using the red light source (12 mW, 633 nm), the normalized current amplitude of micro spot focused by objective lens of 20X was shown in Fig. 4-14 (a). Two orthogonal scanning can be clearly seen in 4-14 (a), where an average current was used for the positive and negative scan. As mentioned in Section 2.3, the power distribution can be acquired from the differentiation of the photocurrent. With a running average filter of 5 point, both the positive scan and negative scan are shown in Fig. 4-14 (b). The aberration due to focusing objective lens is detected. It is a reasonable result as it was also observed from the CCD camera (Fig. 4-10).

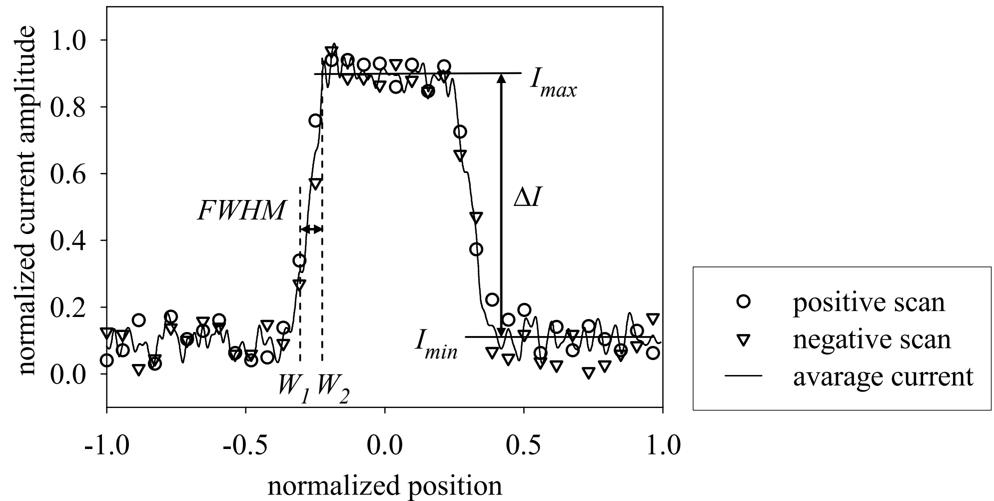

(a) Measured photocurrent amplitude

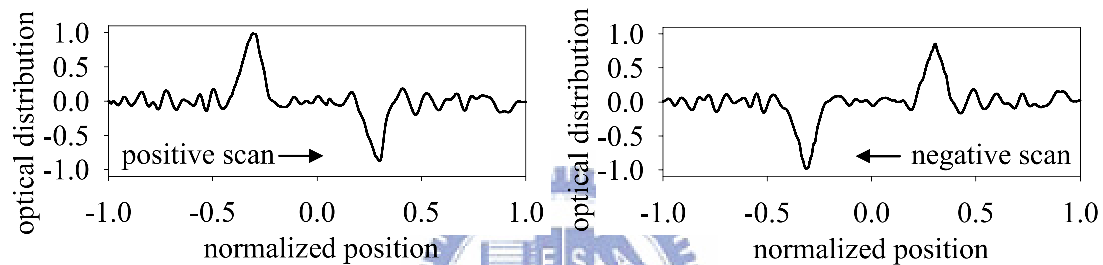

(b) Power distribution in two orthogonal scans

Fig. 4-16 (a) Measured photocurrent and (b) derived power distribution of the spot with 20X objective lens for the green light

With the same light source and signal processing, the normalized photocurrent and power distribution of spot focused by 40X objective lens are shown in Fig. 4-15 (a) and (b). A better focused spot profile (ideal Gaussian distribution) can be achieved when the aperture of objectives is fully covered by laser beam. Practically, the laser beam is larger than the aperture of 40X but less than 20X objectives. Therefore, fine results are observed in Fig. 4-15.

The measured spot size and profile with green light laser are shown in Fig. 4-16 and Fig. 4-17. Although the results were suffered from high frequency noise, the spot size can still be calculated using average current for the maximum and minimum values.

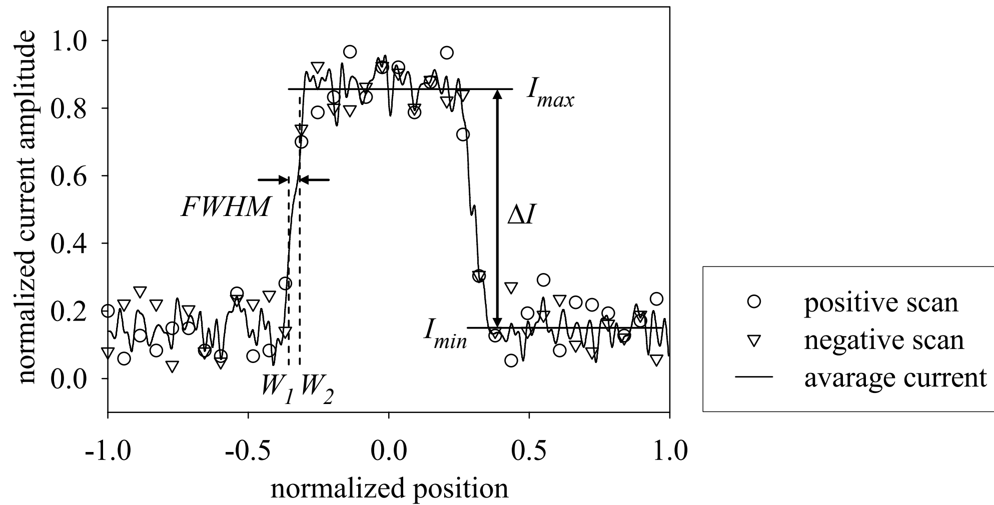

(a) Measured photocurrent amplitude

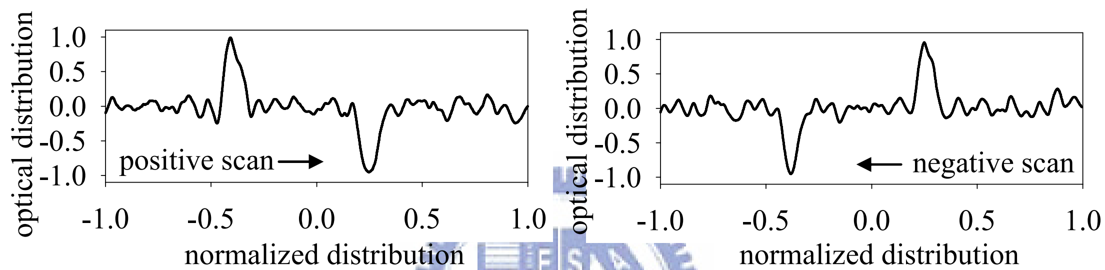

(b) Power distribution in two orthogonal scans

Fig. 4-17 (a) Measured photocurrent and (b) derived power distribution of the spot with 40X objective lens for the green light

To acquire the measured micro spot sizes, the maximum and minimum values of photocurrent, I_{max} and I_{min}, are found at the normalized photocurrent amplitude. By the FWHM definition, the measured spot size is equal to W_2-W_1, where W_1 and W_2 are the positions corresponding to $I_{max}-0.12\Delta I$ and $I_{min}+0.12\Delta I$, and ΔI is the difference of I_{max} and I_{min}. The theoretical spot size can be calculated from Eq. 22. For the 20X and 40X objectives, the NA's are 0.4 and 0.65, respectively. The measurement and calculation results are listed in Table 4-1. Larger focused spot size was measured instead of the minimum theoretical values. It is believed that the spot may had not been focused yet, because it is hard to control the reflection type device precisely positioned at the focused plane.

Table 4-1 Measured and theoretical focused spot size

	wavelength	laser power	objectives	NA	$S_{theoretical}$	$S_{measured}$
1	633 nm	5mW	20X	0.4	0.79 μm	0.9 μm
2	633 nm	5mW	40X	0.65	0.53 μm	0.57 μm
3	543 nm	0.8mW	20X	0.4	0.68 μm	0.82 μm
4	543 nm	0.8mW	40X	0.65	0.44 μm	0.5 μm

In summary, the reflection type device is demonstrated and the preliminary results show the measured spot sizes are close to the theoretical values.

4.3.2 Absorption-type system

The measurement setup of the absorption type device is the same as the reflection type. Instead of the external photo detector, the optical sensor is fabricated on the device to measure the focused spot directly. The generated photocurrent I_a was measured through a series resistor R_L. As shown in Fig. 4-18, the output voltage V_a can be found as the photocurrent I_a under the bias voltage V_{bias} pass through the load resistance. To obtain a large amplification, a tranceimpedance R_L of 1MΩ was used and V_a was observed in the oscilloscope. With V_{bias}= 6V, V_a was equal to 2V with light on and 6V with light off, respectively. Therefore, a photocurrent about 4 μm was measured.

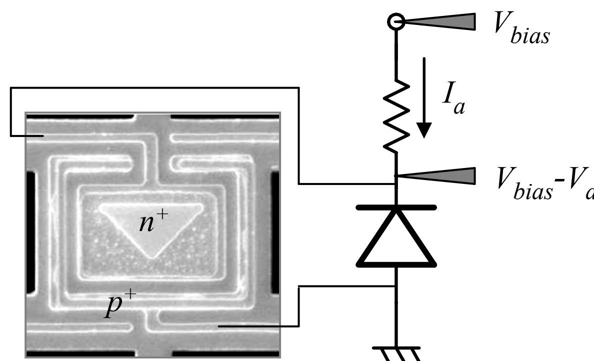

Fig. 4-18 Amplified detection setup

The focused spot scanning was then performed similarly as discussed in the reflection type. However, signal coupling was serious and dominanted the measured waveform. With a driving sinusoidal wave of V_{DC} =15V, V_{AC} =15V at the same frequency, a 1.6V peak-to-peak voltage was found. Therefore, it was necessary to reduce the coupling in the measurement path to obtain an acceptable signal for spot measurement. Since the conduction layers and lines are all isolated by oxide and nitride, the coupling type is the radiated interference where the air is the media (Fig. 4-19). Thus, the main coupling paths in the measurement system were found and eliminated by a ground shielding technique. The near by mechanical structures of floating voltage were also connected to ground to reduce the coupling. Mostly coupling paths were removed as the remains were fabricated inside the chip and hard to remove. Finally, the interference was decreased to about 300 mV peak-to-peak voltage which is a acceptable result.

Despite the each component on the device is normally work, the acquired waveform was unreasonable. As the focused spot was scanned and measured by the reflection type device, however, the detected current of the photodiode on comb had no obvious differences. To figure out the operation of knife edge detector, the device

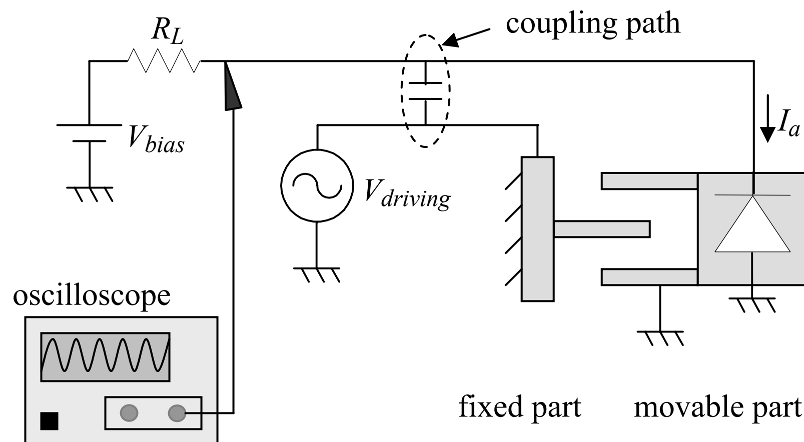

Fig. 4-19 Coupling of the absorption type device

was moved by the position stage instead of the vibration at resonance. The results showed the optical power was sensed not only at the triangular detection region but also at the other part, such as finger, whereas the detected amplitude was smaller by a factor of 0.8. Therefore, the power distribution of the focused spot can not be derived. The reason of the unexpected result is still unknown and further test of the components are in progress.

4.4 Summary

In this chapter, the resonance amplitude and frequency of the SOI device was measured. The measured properties of the comb were close to the theoretical value and verified the actuator design successfully.

The photocurrent of the fabricated detector was measured. The results of each run and each process were compared and discussed.

The reflection type system was used to measure the focused laser spot size. The preliminary results showed relatively good agreement with the theoretical values. Finally, test experiments on the absorption device are still performed to find out a reasonable explain.

Chapter 5 Conclusion and Future Work

5.1 Conclusion

In this thesis, a MEMS-based optical spot profile measurement system was designed and fabricated. The SOI and CMOS post process are proposed for the reflection and absorption type devices. Besides, a new approach for backside etching is proposed to improve the yield of fabrication. The fabricated comb actuator has a ±10 μm displacement at resonant frequency of 7.13 kHz which is very close to the original design. The characteristics of the fabricated photo detector were measured and discussed.

The measurements of the reflection type devices demonstrate the micro optical spot profile measurement system. Similar results to the theoretical spot size and profile were acquired with different light sources and objective lens. The reasons and the solutions to the encountered problems in the absorption type measurement are still searching.

5.2 Future work

The improvements for the fabricated devices are discussed. During the fabrication, aluminum layer was easily peeled-off due to its bad adhesion. As a result, many absorption type devices were unusable while the device can not operated with no conduction paths. Therefore, an adhesion layer like Ti should be evaporated before Al coating to increase the yield of the fabrication.

Although the coupling problem in the absorption type is finally reduced to an acceptable value of 300 mV, a practical solution at design level is considered more effective. As the main coupling effect is found most serious at the pins of PCB, the

wired lines of the pins for driving sinusoidal signal and the bias voltage should be apart to reduce the coupling. Besides, keeping the pads on chip far away from layout design is also concerned necessarily.

In the absorption type measurement, a transimpedance amplifier (TIA) is used to convert the input current (generated by the photo detector) to the readout voltage. Using CMOS and its post process, a fully integration with TIA circuits can be achieved. The signal paths between components can be conducted by the remained three metal layers after post fabrication. A new CMOS device integrated with TIA circuits is in progress.

By the proposed system, a high resolution measurement of the focused spot size can be achieved. However, the accuracy of the actuator may degrade due to the mechanical fatigue over long time of operation. Therefore, a piezoresistive sensor for measuring the comb displacement will be integrated into the device. Once the decreased scanning range is detected by the sensor, a compensated voltage can be applied to feedback control the scanning of the knife edge plate precisely.

References

[1] J. Hsu, "Near-field scanning optical microscopy studies of electronic and photonic materials and devices," *Materials Science & Engineering,* vol.R33, no.1, pp. 1-50, 2001.

[2] G.K. Fedder, S. Santhanam, M.L. Reed, S.C. Eagle, D.F. Guillou, MS-C Lu, L.R. Carley, "Laminated high-aspect-ratio microstructures in a conventional CMOS process," *Sensors and Actuators A (Physical),* vol.A57, no.2, pp. 103-10, 1996.

[3] H. Luo, G.K. Fedder, L.R. Carley, "A 1 mG lateral CMOS-MEMS accelerometer," *Proceedings IEEE Thirteenth International Conference on Micro Electro Mechanical Systems IEEE.* pp. 502-7, 2000.

[4] H. Luo, X. Zhu, H. Lakdawala, L.R. Carley, G.K. Fedder, "A copper CMOS -MEMS Z-axis gyroscope," *Proceedings IEEE Fifteenth International Conference on Micro Electro Mechanical Systems. IEEE.* pp. 631-4, 2002.

[5] H. Lakdawala, G.K. Fedder, "CMOS micromachined infrared imager pixel," *TRANSDUCERS '01. 11th International Conference on Solid-State Sensors and Actuators.* Part vol.1, pp. 556-9 vol.1, 2001.

[6] H. Xie, L. Edermann, Q. Jing, G.K. Fedder, "Simulation and characterization of a CMOS z-axis microactuator with electrostatic comb drives," *Proceedings International Conference on Modeling and Simulation of Microsystems,* 27-29, pp.181-184, 2000.

[7] T. Sziranyi, P. Barczikay, T. Kovacs, "Measurement theory of laser-beam diameter of about 1 μm by moving CCD sensor," *International Journal of Optoelectronics,* vol.3, no.2, pp. 187-94, 1988.

[8] Y.H. Fu, F.H. Ho, W.C. Lin, W-C Liu, D.P. Tsai, "Study of the focused laser spots generated by various polarized laser beam conditions," *Journal of Microscopy,* vol.210, pp. 225-8, 2003.

[9] M. Cywiak, M. Servin, F. M. Santoyo, "Vibrating knife-edge technique for measuring the focal length of a microlens," *Applied Optics,* vol.40, no.28, pp.

4947-52, 2001.

[10] M.N. Variyam, "Behavior of a MOEMS package (Ti DMD™) under mechanical and thermal loads," *Micro-Electro-Mechanical Systems (MEMS). 2000 ASME International Mechanical Engineering Congress and Exposition. ASME.* pp. 601-8, 2000.

[11] M. Sasaki, K. Tanaka, K Hane, "Cantilever probe integrated with light-emitting diode, waveguide, aperture, and photodiode for scanning near-field optical microscope," *Japanese Journal of Applied Physics,* Part 1, vol.39, no.12B, pp. 7150-3, 2000.

[12] K. Hane, T. Endo, Y. Ito, M. Sasaki, "A compact optical encoder with micromachined photodetector," *Journal of Optics A: Pure and Applied Optics,* vol.3, no.3, pp. 191-5, 2001.

[13] S.H. Kong, G. de Graaf, R.F. Wolffenbuttel, "Spectral performance of a silicon IR microspectrometer," *12th International Conference on Solid-State Sensors, Actuators and Microsystems. IEEE.* Part vol.2, pp. 1610-13, 2003.

[14] H. Xie, L. Erdmann, X. Zhu, K.J. Gabriel, G.K. Fedder, "Post-CMOS processing for high-aspect-ratio integrated silicon microstructures," *IEEE/ASME Journal of Microelectro -mechanical Systems,* vol.11, no.2, pp. 93-101, 2002.

[15] H. Xie, G.K. Fedder, "A CMOS-MEMS lateral-axis gyroscope," *MEMS 2001. Proceedings IEEE Fifteenth International Conference on Micro Electro Mechanical Systems. IEEE.* pp. 162-5, 2001.

[16] A. Jain, A. Kopa, Y.T. Pan, G.K. Fedder, H. Xie, "A two-axis electrothermal micromirror for endoscopic optical coherence tomography," *IEEE Journal of Selected Topics in Quantum Electronics,* vol.10, no.3, pp. 636-42, 2004.

[17] V.A. Shilin, P.A. Skrylev, A.L. Stempkovsky, "Optimization of CMOS APS pixel," *Proceedings SPIE,* vol. 5049, pp. 670-8, 2003.

[18] R. Legtenberg, A.W. Groeneveld, M. Elwenspoek, "Comb-drive actuators for large displacements," *Journal of Micromechanics and Microengineering,* vol.6, no.3, pp. 320-9, 1996.

[19] R.K. Gupta, "Electronically probed measurements of MEMS geometries," *IEEE/ASME Journal of Microelectromechanical Systems,* vol.9, no.3, pp. 380-9, 2000.

[20] W.C. Tang, M.G. Lim, R.T. Howe, "Electrostatic comb drive levitation and control method," *IEEE/ASME Journal of Microelectromechanical Systems,* vol.1, no.4, pp. 170-8, 1992.

[21] W.C. Tang, C. Tu, H. Nguyen, R.T. Howe, "Laterally driven polysilicon resonant microstructures," *Sensors and Actuators,* vol.20, no.1-2, pp. 25-32, 1989.

[22] W.A. Johnson, L.K.Warne, "Electrophysics of micromechanical comb actuators," *IEEE/ASME Journal of Microelectromechanical Systems,* vol.4, no.1, pp. 49-59, 1995.

[23] G.K. Fedder, T. Mukherjee, "Physical design for surface-micromachined MEMS," *Proceedings ACM/SIGDA fifth Physical Design Workshop, Reston, VA USA,* pp. 53-60, 1996.

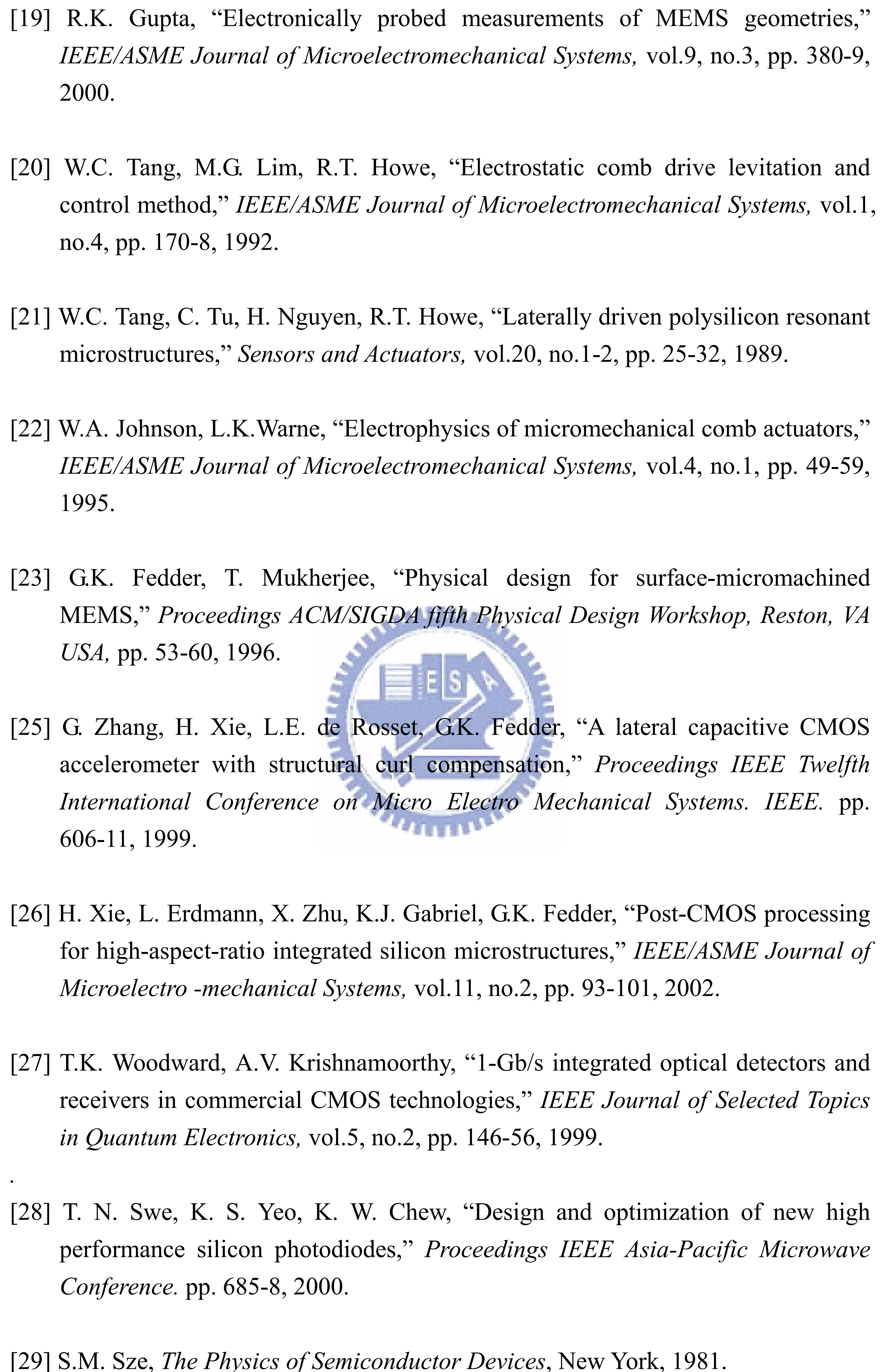

[25] G. Zhang, H. Xie, L.E. de Rosset, G.K. Fedder, "A lateral capacitive CMOS accelerometer with structural curl compensation," *Proceedings IEEE Twelfth International Conference on Micro Electro Mechanical Systems. IEEE.* pp. 606-11, 1999.

[26] H. Xie, L. Erdmann, X. Zhu, K.J. Gabriel, G.K. Fedder, "Post-CMOS processing for high-aspect-ratio integrated silicon microstructures," *IEEE/ASME Journal of Microelectro -mechanical Systems,* vol.11, no.2, pp. 93-101, 2002.

[27] T.K. Woodward, A.V. Krishnamoorthy, "1-Gb/s integrated optical detectors and receivers in commercial CMOS technologies," *IEEE Journal of Selected Topics in Quantum Electronics,* vol.5, no.2, pp. 146-56, 1999.

.

[28] T. N. Swe, K. S. Yeo, K. W. Chew, "Design and optimization of new high performance silicon photodiodes," *Proceedings IEEE Asia-Pacific Microwave Conference.* pp. 685-8, 2000.

[29] S.M. Sze, *The Physics of Semiconductor Devices*, New York, 1981.

[30] R.F. Pierret, *Semiconductor Device Fundamentals*, Addision-Wesley, 1996.

[31] R.A. Sinton, A. Cuevas, "Contactless determination of current-voltage characteristics and minority-carrier lifetimes in semiconductors from quasi-steady-state photoconductance data," *Applied Physics Letters,* vol.69, no.17, pp. 2510-12, 1996.

[32] N. Belov, N. Khe, "Using deep RIE for micromachining SOI wafers," *Proceedings Electronic Components and Technology Conference 2002. IEEE.* pp. 1163-6, 2002.

[33] W. Chu, M. Mehregany, D. Hansford, P. Pirouz, "Effect of thermal oxidation on residual stress distribution through the thickness of p^+ silicon films," *Proceedings IEEE Solid-State Sensor and Actuator Workshop.* pp. 90-3, 1992.

[34] X. Zhu, "Post-CMOS Micromachining of Surface and Bulk Structures" *ph.D thesis, Department of Electrical and Computer Sciences, Carnegie Mellon University, Pittsburgh, PA,* 2002.

[35] H. Urey, "Spot size, depth-of-focus, and diffraction ring intensity formulas for truncated Gaussian beams," *Applied Optics,* vol.43, no.3, pp. 620-5, 2004.